

The CHIME Pulsar Project: System Overview

CHIME/PULSAR COLLABORATION, M. AMIRI,¹ K. M. BANDURA,^{2,3} P. J. BOYLE,^{4,5} C. BRAR,^{4,5} J.-F. CLICHE,^{4,5} K. CROWTER,¹ D. CUBRANIC,¹ P. B. DEMOREST,⁶ N. T. DENMAN,⁷ M. DOBBS,^{4,5} F. Q. DONG,¹ M. FANDINO,¹ E. FONSECA,^{4,5} D. C. GOOD,¹ M. HALPERN,¹ A. S. HILL,^{8,9} C. HÖFER,¹ V. M. KASPI,^{4,5} T. L. LANDECKER,⁹ C. LEUNG,^{10,11} H.-H. LIN,^{12,13} J. LUO,¹² K. W. MASUI,^{10,11} J. W. MCKEE,¹² J. MENA-PARRA,¹⁰ B. W. MEYERS,¹ D. MICHILLI,^{4,5} A. NAIDU,^{4,5} L. NEWBURGH,¹⁴ C. NG,¹⁵ C. PATEL,^{15,4} T. PINSONNEAULT-MAROTTE,¹ S. M. RANSOM,¹⁶ A. RENARD,¹⁵ P. SCHOLZ,¹⁵ J. R. SHAW,¹ A. E. SIKORA,^{4,5} I. H. STAIRS,¹ C. M. TAN,^{4,5} S. P. TENDULKAR,^{4,5} I. TRETYAKOV,^{15,17} K. VANDERLINDE,^{18,15} H. WANG,^{10,11} AND X. WANG¹⁹

¹Department of Physics & Astronomy, University of British Columbia, 6224 Agricultural Road, Vancouver, BC V6T 1Z1, Canada

²CSEE, West Virginia University, Morgantown, WV 26505, USA

³Center for Gravitational Waves and Cosmology, West Virginia University, Morgantown, WV 26505, USA

⁴Department of Physics, McGill University, 3600 rue University, Montréal, QC H3A 2T8, Canada

⁵McGill Space Institute, McGill University, 3550 rue University, Montréal, QC H3A 2A7, Canada

⁶National Radio Astronomy Observatory, P.O. Box O, Socorro, NM 87801 USA

⁷Central Development Laboratory, National Radio Astronomy Observatory, 1180 Boxwood Estate Road, Charlottesville, VA USA 22903

⁸Department of Computer Science, Math, Physics, and Statistics, University of British Columbia, 3187 University Way, Kelowna, BC V1V 1V7, Canada

⁹National Research Council Canada, Herzberg Research Centre for Astronomy and Astrophysics, Dominion Radio Astrophysical Observatory, PO Box 248, Penticton BC V2A 6J9, Canada

¹⁰MIT Kavli Institute for Astrophysics and Space Research, Massachusetts Institute of Technology, 77 Massachusetts Ave, Cambridge, MA 02139, USA

¹¹Department of Physics, Massachusetts Institute of Technology, 77 Massachusetts Ave, Cambridge, MA 02139, USA

¹²Canadian Institute for Theoretical Astrophysics, 60 St. George Street, Toronto, ON M5S 3H8, Canada

¹³Max Planck Institute for Radio Astronomy, Auf dem Huegel 69, 53121 Bonn, Germany

¹⁴Department of Physics, Yale University, New Haven, CT 06520, USA

¹⁵Dunlap Institute for Astronomy & Astrophysics, University of Toronto, 50 St. George Street, Toronto, ON M5S 3H4, Canada

¹⁶National Radio Astronomy Observatory, 520 Edgemont Rd., Charlottesville, VA 22903, USA

¹⁷Department of Physics, University of Toronto, Toronto, Ontario, M5S 3H4, Canada

¹⁸David A. Dunlap Department of Astronomy & Astrophysics, University of Toronto, 50 St. George Street, Toronto, ON M5S 3H4, Canada

¹⁹School of Physics and Astronomy, Sun Yat-sen University, 2 Daxue Road, Zhuhai, China

(Received XXX; Revised YYY; Accepted ZZZ)

ABSTRACT

We present the design, implementation, and performance of the digital pulsar observing system constructed for the Canadian Hydrogen Intensity Mapping Experiment (CHIME). Using accelerated computing, this system processes independent, digitally-steered beams formed by the CHIME correlator to simultaneously observe up to 10 radio pulsars and transient sources. Each of these independent streams are processed by the CHIME/Pulsar backend system which can coherently dedisperse, in real time, up to dispersion measure values of 2500 pc cm^{-3} . The tracking beams and real-time analysis system are autonomously controlled by a priority-based algorithm that schedules both known sources and positions of interest for observation with observing cadences as rapid as one day. Given the distribution of known pulsars and radio-transient sources, and the dynamic scheduling, the CHIME/Pulsar system can monitor 400–500 positions once per sidereal day and observe most sources with declinations greater than -20° once every ~ 4 weeks. We also discuss the extensive science program enabled

through the current modes of data acquisition for CHIME/Pulsar that centers on timing and searching experiments.

Keywords: instrumentation: interferometers – methods: observational – radio continuum: general – pulsars: general – techniques: interferometric – telescopes

1. INTRODUCTION

The Canadian Hydrogen Intensity Mapping Experiment (CHIME¹) is a radio interferometer operating in the 400–800 MHz frequency range, located at the Dominion Radio Astrophysical Observatory (DRAO) in Penticton, British Columbia, Canada. CHIME is a wide-field transit telescope with no physical-slew capabilities, with a primary design goal to study dark energy through the measurement of the evolution of baryon acoustic oscillations across the redshift range of $0.8 < z < 2.5$. This measurement will be accomplished by mapping neutral-hydrogen emission as a function of frequency across the entire Northern sky. From initial conception, it was realized that the CHIME telescope is also highly suitable for high-cadence observations of radio pulsars, while later planning and development was undertaken to enable untargeted searches for fast radio bursts (FRBs; see e.g. Lorimer et al. 2007; Thornton et al. 2013; Petroff et al. 2019). To date, several telescope backends have been developed for CHIME that perform pulsar and FRB observations, as well as very-long baseline interferometry (VLBI) and forthcoming measurements of neutral-hydrogen absorption systems (Yu et al. 2014). In this work, we describe the design, performance, and motivation of a pulsar-timing system constructed for CHIME, hereafter referred to as CHIME/Pulsar.

CHIME and the CHIME/Pulsar system differ from other radio observatories in two distinct ways: CHIME/Pulsar observes up to 10 different celestial positions at any instant in time, capable of acquiring spectro-temporal data in two different acquisition modes commonly used in pulsar and FRB astronomy; and CHIME/Pulsar is designed to observe continuously with the CHIME FX correlator, and commensally with other CHIME backends. These two capabilities allow CHIME/Pulsar to observe 400–500 known pulsars per day, and nearly all known sources in the the CHIME field of view (i.e., $\delta > -20^\circ$) within one month. CHIME therefore acts as an automated, high-cadence observatory for pulsar science.

Until recently, only a small fraction of the ~ 2800 known radio pulsars was observed regularly using other

radio facilities due to competitive and limited telescope resources. Nonetheless, high-cadence observations of many millisecond pulsars (MSPs) have been projected to: boost sensitivity towards nearby, resolvable sources of nanohertz-frequency gravitational waves (GWs) emitted from merging galaxies (e.g. Christy et al. 2014); resolve abrupt temporal variations in dispersion properties that reflect a complex interstellar medium (ISM; e.g., Lam et al. 2018); and constrain the equation of state of ultra-dense matter (e.g. Demorest et al. 2010). Furthermore, high precision timing of an array of many stable MSPs is being used to search for, and directly detect, the low frequency GW background (e.g. Verbiest et al. 2016; Perera et al. 2019), a concept commonly referred to as a “pulsar timing array” (PTA).

Renewed and frequent tracking of historically low-priority sources will likely resolve dynamical processes affecting pulsar rotation, such as unidentified long-period orbital motion (Kaplan et al. 2016; Bassa et al. 2016; Antoniadis 2021) and many pulsar “glitches” (e.g. Espinoza et al. 2011). The CHIME/Pulsar system is also effective at monitoring sporadically emitting pulsars and other transient events that can provide great insight into pulsar emission intermittency and astrophysical coherent radio emission mechanisms more broadly. The ability of CHIME/Pulsar to monitor the entire Northern-hemisphere pulsar population on a regular basis is therefore expected to yield unprecedented access to a large number of timing-based phenomena that previously could not be resolved elsewhere.

A brief introduction to the CHIME/Pulsar project has been presented by Ng & CHIME/Pulsar Collaboration (2017). Here we provide a more detailed overview of the CHIME/Pulsar system, its placement within the CHIME infrastructure, the performance of CHIME/Pulsar, and science topics to be addressed with the CHIME/Pulsar system. In Section 2, we describe the hardware components of the CHIME instruments and the pulsar-timing backend. In Section 3, we provide an overview of the software suite developed to make pulsar-timing measurements possible with CHIME. In Section 4, we outline the current performance of the CHIME/Pulsar system and provide a sample of preliminary results in demonstration of CHIME’s capabilities as a pulsar-timing observatory. In Section 5, we discuss various scientific opportunities enabled by

¹ <https://chime-experiment.ca>

the CHIME/Pulsar system. Finally, we summarize this work and its anticipated science outcomes in Section 6.

2. HARDWARE

CHIME consists of 1024 dual-polarization radio-frequency inputs coupled to a correlator and then several independent backend digital instruments. Here we briefly describe the major signal-chain components relevant to the CHIME/Pulsar project. See Figure 1 for a schematic diagram of the signal chain from the receivers to the CHIME/Pulsar backend.

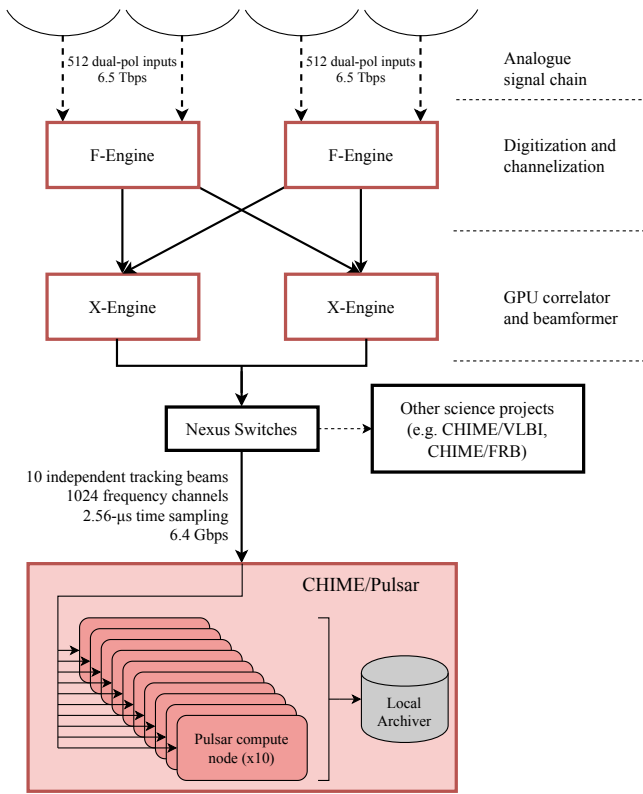


Figure 1. Schematic of the CHIME telescope signal path. The telescope structure (four cylinders, here black arcs), the correlator (F- and X-Engines), and the CHIME/Pulsar backend are shown. The dashed black lines represent coaxial cables carrying the analogue signal from the 256 feeds on each cylinder to the F-Engines in the East/West receiver enclosures, situated below the telescope. The total input data rate into the F-Engine is 13 Tbps. The solid black lines depict digitized data carried through copper and/or fiber-optic cables. Networking devices between the F- and X-Engines are not shown. The X-Engine (GPU-based correlation and beamforming) is housed in two shipping containers adjacent to the cylinders. The CHIME/Pulsar backend (shaded red) is housed in a shielded room in the DRAO building. The data rate into the CHIME/Pulsar backend is 6.4 Gbps.

2.1. Telescope Structure and Receiver

The CHIME telescope consists of four 5-m focal length parabolic cylinders that are 20 m wide and 100 m long. The cylinders are oriented North-South, each mounted with 256 dual-polarization ‘cloverleaf’ antennas (Deng & Campbell-Wilson 2014) placed 30 cm apart below a 68 cm-wide groundplane at the parabolic focus. Two low noise amplifiers are coupled directly to each antenna. These are coupled via 60 m of low-loss coaxial cables to custom band-defining filter-amplifiers located in a radio-frequency shielded room containing analog-to-digital converters and the frequency channelization portion of the CHIME correlator. Basic telescope properties are given in Table 1.

Table 1. Telescope specifications.

Field of view	120° (N-S) 1.3–2.5° (E-W)
Receiver noise temperature	~50 K (nominal)
Frequency range	400–800 MHz
Polarization basis	orthogonal linear
Telescope longitude	−119°37'25.238"
Telescope latitude	49°19'14.553"
Telescope elevation ^a	547.918 m

^aAbove the GRS 80 ellipsoid.

2.2. FX Correlator

CHIME employs a hybrid FX correlator that consists of custom-built electronics and adapted commodity processing units. The first stage, known as the F-Engine, is responsible for signal digitization and frequency separation, while the second stage, X-Engine, is responsible for spatial correlation and beamforming.

2.2.1. F-Engine: Digitization and Channelization

The amplified input signals are digitized and separated into 1024 frequency channels, resulting in a spectral resolution of 390 kHz, by the F-Engine system. The details of the F-Engine are presented in Bandura et al. (2016) and are discussed further in CHIME/FRB Collaboration et al. (2018). In summary, the F-Engine consists of 128 “ICE” FPGA-based motherboards where the signals from the 1024 dual-polarization receivers are digitized at 800 million samples per second with 8-bit precision. The baseband streams are channelized by a 4-tap polyphase filterbank into 1024 frequency channels. The positive frequency spectra of these channelized data are rounded to (4+4)-bit complex numbers after applying a programmable gain and phase offset, which halves the input data rate of 13.1 Tbps to 6.5 Tbps. The complex-voltage data are further re-organized to form 1024 data

streams, which are transmitted via fibre-optic connection to the next processing stage.

2.2.2. *X-Engine: GPU Correlator and Beamformer*

The CHIME correlator X-Engine is a computing cluster consisting of 256 nodes hosting a total of 512 dual-chip AMD FirePro 9300 X2 graphics processing units (GPUs). These nodes are divided between two emission-shielded shipping containers located on the east side of the CHIME reflectors. Each X-Engine node processes four frequency channels – one frequency per GPU chip – for each of the 1024 dual-polarization receiver inputs. A set of GPU kernels process the input data to manipulate the CHIME baseband into a variety of data products required by downstream backends. The kernel used by CHIME/Pulsar system is discussed in Section 3.1. The X-Engine data products are exported from the nodes over Gigabit Ethernet (GbE) to a set of commercially-available network switches, and then to various backend systems. A full description of the CHIME X-Engine and its capabilities is given by Denman et al. (2020).

2.3. *CHIME/Pulsar Backend*

The CHIME/Pulsar backend consists of ten independent compute nodes that are connected directly to the CHIME correlator through a series of network switches. Each compute node consists of a Supermicro motherboard, an Intel Xeon E5-1650 central processing unit (CPU), 128 GB of RAM, and a solid-state drive (SSD). Data are received through a 10-Gbps Intel Network Interface Controller (NIC) and is temporarily buffered in RAM before being processed through an FFT-based coherent dedispersion algorithm on a single, liquid-cooled NVIDIA Titan X GPU. The resulting data are temporarily stored and further processed on a local, 60-TB data archiver.

2.4. *Local Data-archiving Server*

The CHIME/Pulsar backend ultimately writes a variety of data products with variable file sizes several hundred times every sidereal day, at a time-averaged rate of 67 Mbps. In order to handle the output data rate, we built a local data-archive server using components similar to the hardware described above. The archiving server employs two redundant arrays of independent disks (RAIDs) for secure, short-term storage of CHIME/Pulsar data products. This short-term data archive can accommodate several months of continuous typical data acquisition, and is sufficient in the event that higher data-rate modes (see Section 3.3) become emphasized for a moderate time span. These data are eventually transferred offsite via ground shipment

of physical hard drives to CHIME/Pulsar institutions for uploading to multi-purpose computing facilities for offline processing and long-term preservation. The primary long-term data archiving occurs on the Cedar cluster of Compute Canada².

3. SOFTWARE

Here we describe the suite of software tools we have developed and implemented for rendering sky signals from the FX correlator into useful CHIME/Pulsar data products. Salient details of the CHIME/Pulsar backend output are given in Table 2.

3.1. *Beamforming and Calibration*

We digitally form 10 dual-polarization tied-array beams within the X-Engine by summing all 1024 inputs phased to specified celestial coordinates. The 10 independent beams allow for tracking of 10 different sky positions simultaneously within the primary beam of CHIME. The re-pointing of each beam is performed over the network using the Representational State Transfer (REST) application programming interface, and typically occurs within milliseconds of command execution.

The complex gain calibration (amplitude and phase) of the input data is achieved via point-source calibration with bright continuum sources such as Cas A, Cyg A, and Tau A (CHIME Collaboration et al., in prep.). During a bright continuum source transit, the visibility matrix for CHIME is treated as approximately the product of the complex gain and sky signal (as viewed through the beam response function). In this limit, computing an eigendecomposition of the visibility matrix allows us to determine the complex gain for each antenna at each frequency channel in the direction of the calibrator source. The eigenvectors corresponding to the two largest eigenvalues represent the complex gains for the X and Y polarizations of each input. After determining the eigenvectors, we also remove known interferometric phase based on the physical separation of the antennas by a process known as fringe-stopping (e.g. Thompson et al. 2001).

As part of the calibration process, data from poorly behaving antennas and contaminated frequencies are masked. A static list of inputs which are known to be malfunctioning are removed and this list is updated on a daily basis. Calibration solutions with more than 5% of inputs deemed bad are flagged as poor quality, and the most recent, preceding solutions deemed adequate are instead used until the next calibrator transit occurs. While radio frequency interference (RFI) excision

² <https://www.computecanada.ca>

Table 2. CHIME/Pulsar data specifications.

Number of tied-array beams	10
Beam width (FWHM)	$\sim 0.5^\circ$ (at 400 MHz) $\sim 0.25^\circ$ (at 800 MHz)
Number of spectral channels	1024
Frequency resolution	390.625 kHz
Time resolution	2.56 μ s (baseband) 327.68 μ s (output filterbank)
Output data bit depth	8
Number of profile bins ^a	256/512/1024/2048 (fold-mode)
Output polarization state	Full Stokes (fold-mode) Total intensity (filterbank)
Pulsar data output rate ^b	X, Y (baseband) 67 Mbps

^aConfigurable options set when scheduling observations.

^bTime-averaged over a typical observing day.

in CHIME data can be a serious challenge, some channels are known to always be contaminated, and these channels are masked in the calibration solutions.

During the “pre-commissioning” period of CHIME operations (before August 2018), phase-only calibration was computed every few days. Since September 2018, daily amplitude and phase calibration solutions have been calculated.

3.2. Data packet format, transfer and assembly

For each X-Engine GPU node, the resulting beamformed data from each of the four processed frequency channels are scaled down, encoded into (4+4)-bit complex numbers, and packetized in VLBI Data Interchange Format (VDIF)³. Each individual packet consists of 625 samples of one of the two polarizations for each of the four frequency channels and a VDIF header of 32 bytes, resulting in a total packet size of 5032 bytes. The corresponding pulsar data rate on each FX-correlator node for all 10 beams is 0.2516 Gbps, with a total network load of \sim 64 Gbps for all pulsar beams. Each individual pulsar-backend node receives \sim 6.4 Gbps of data from the correlator in the form of User Datagram Protocol (UDP) packets. The incoming data rate to each pulsar nodes corresponds to 1.6×10^5 packets per second. We have optimized our network-capture algorithms in order to properly receive packets with negligible packet loss⁴. The received packets are assembled and written to memory in preparation of further processing.

3.3. Data processing

The main purpose of the CHIME/Pulsar system is to autonomously monitor radio pulsars with regular cadence. The beamformed dual-polarization timeseries are coherently dedispersed and processed to form the data product defined by the scheduled observation configuration. Most observations occur in “fold mode,” where the dedispersed baseband data are manipulated to yield time-averaged pulse profiles for all 1024 frequency channels over a specified integration time, using a set of pulsar rotation parameters for coherent averaging of the signal. In most cases, the number of profile phase bins for a given fold-mode observation is 256, although this number is nominally defined by the science case and, therefore, dictated by the scheduling process. By default, 10-second integrations are formed for all fold-mode observations, although this could in principle be adjusted on a per-pulsar basis. When desired, observations may also be conducted in “filterbank mode,” where the dedispersed baseband timeseries are converted into a Stokes- I data stream that is then downsampled in time. In special circumstances, it is scientifically worthwhile to directly record beamformed baseband data for specific pulsars and FRBs of interest. We have developed the appropriate software capabilities to enable all three types of observation with the CHIME/Pulsar system. The basic output data specifications of the CHIME/Pulsar system are given in Table 2.

3.3.1. Fold mode

For fold-mode observations, the CHIME/Pulsar backend uses the “Digital Signal Processing for Pulsars”

³ <https://vlbi.org/vlbi-standards/vdif>

⁴ The details about the optimizations employed are beyond the scope of this paper, but available upon request.

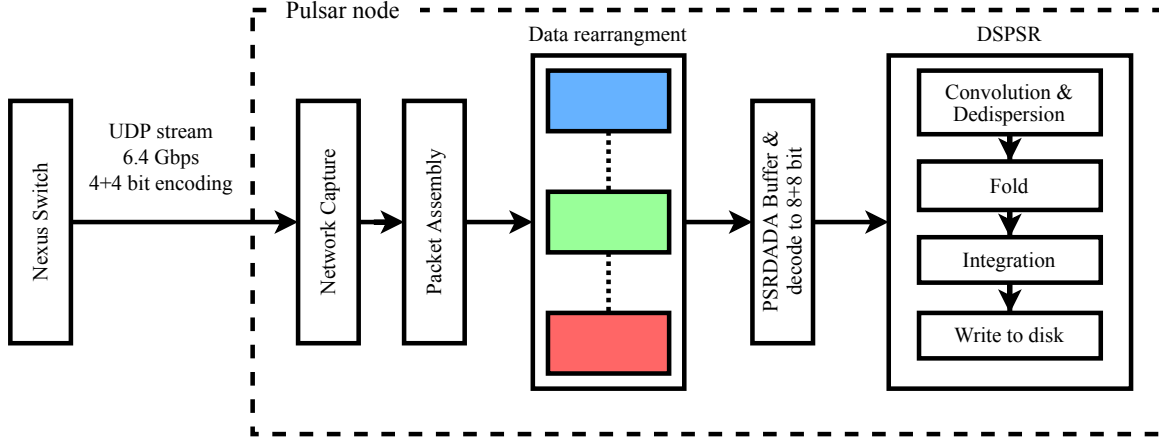


Figure 2. A schematic illustrating the various operations on the data streams from the correlator in fold mode, with colors denoting frequency channels. The unordered UDP packets from the correlator are routed to the specified pulsar node where the data are organized in the assembler stage which involves both network capture and packet assembly. The assembled data, reordered into a polarization-frequency-time series in order of increasing index variation, are then passed on to the DSPSR process using PSRDADA buffers.

(DSPSR) suite⁵, an open source GPU-based library (van Straten & Bailes 2011). Written in C++ and CUDA⁶, DSPSR is a high performance, general-purpose tool for high-time-resolution radio pulsar studies using accelerated computing. DSPSR is used in many astrophysical applications (e.g. Karuppusamy et al. 2012; Martinez et al. 2015; Price et al. 2016) and is extensively used as a part of real-time processing instrumentation for various telescopes around the world.

DSPSR has the ability to read from and write to data buffers created using the PSRDADA library⁷. PSRDADA is an open source software that allows the creation of flexible and well managed ring buffers, with a variety of applications for piping data from process to ring buffer, and vice versa. In addition to enabling transfer of data between processes, PSRDADA provides various utilities to manage data within the ring buffer itself.

For fold-mode observations, the incoming data streams from the CHIME X-Engine are sorted and arranged as a polarization-frequency-time series prior to entering the real-time processing stage. The assembled data are then passed onto the DSPSR process using PSRDADA buffers. Even though it has the ability to accept data with (4+4)-bit encoding, DSPSR runs significantly faster when instead receiving data with (8+8)-bit encoding. We have thus modified the PSRDADA software to convert data to (8+8)-bit encoding before passing them to DSPSR in order to circumvent this is-

sue. Once the data are passed into the DSPSR GPU buffers, DSPSR executes several kernels that perform coherent dedispersion and timing-model folding of the data before writing to disk. A schematic of the processing chain for fold-mode observations is presented in Figure 2.

Output fold-mode data products are written to structured files (“archives”) that are readable by the PSRCHIVE software suite⁸ (Hotan et al. 2004; van Straten et al. 2012) for offline processing and analysis. An example of the CHIME/Pulsar system fold-mode data from an observation of PSR B1937+21 is given in Figure 3.

3.3.2. Filterbank mode

The CHIME/FRB system is discovering many repeating FRBs (CHIME/FRB Collaboration et al. 2019a,b; Fonseca et al. 2020), as well as single pulses from unknown radio pulsars and “rotating radio transients” (RRATs; McLaughlin et al. 2006). Some fraction of the CHIME/Pulsar observing time is thus expected to be used for follow-up observations of these sources. To observe repeating FRB sources, the pulsar backend must be able to record coherently dedispersed high-time-resolution filterbank data. Since these extragalactic sources are known to have DMs upwards of 1000 pc cm^{-3} it is also essential that the backend can support such DM ranges.

The readily available DSPSR filterbank module *digifil* cannot support real-time performance at such large DMs at the CHIME operating frequency range. To overcome

⁵ <http://dpsr.sourceforge.net>

⁶ <https://developer.nvidia.com/cuda-zone>

⁷ <http://psrdada.sourceforge.net>

⁸ <http://psrchive.sourceforge.net>

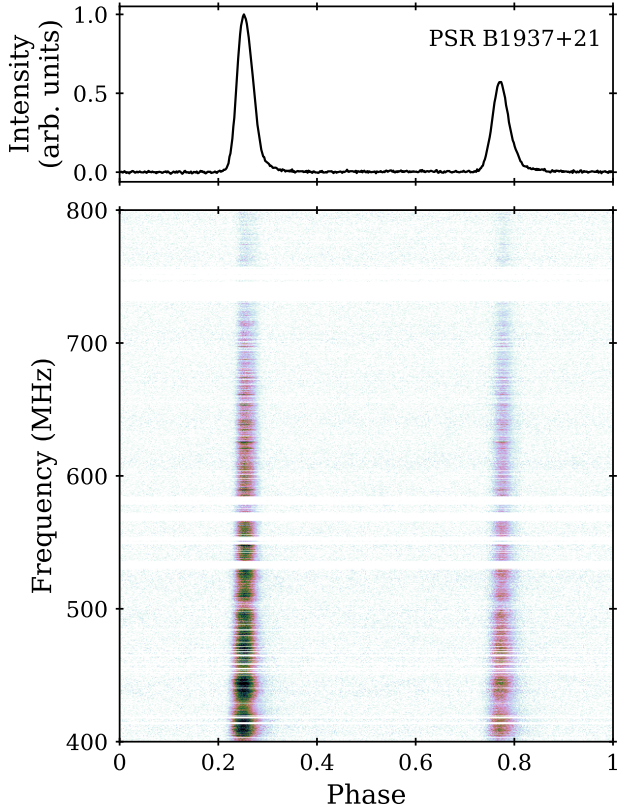


Figure 3. A fold-mode observation of PSR B1937+21. The bottom panel is the phase versus frequency (waterfall) plot, and the top panel is the mean intensity after summing all frequency channels (i.e. the integrated pulse profile). There is clear evidence of pulse broadening due to interstellar scattering visible in the folded profile and as a function of frequency across the 400 MHz bandwidth.

this, we have developed a new codebase for the filterbank mode with the ability to dedisperse incoming data to a maximum DM of 3300 pc cm^{-3} in real-time based on work by Naidu et al. (2015). The significant change in our implementation is the input data format. Based on benchmark tests on FFT performance, the efficiency of the GPUs can be improved by a factor of five if the input data format is changed from polarization-frequency-time series to polarization-time-frequency series as shown in Figure 4.

The received UDP packets are arranged into a polarization-time-frequency series and are passed on to the GPU for coherent dedispersion at a user-specified DM. This dedispersed data are then passed on to the CPU for downsampling, and then manipulated into a community-established filterbank format before writing to disk. All the code for the CPU processes after GPU kernel execution are written in Intel AVX2 intrinsics.

3.4. Scheduler and web monitors

An automated scheduler is necessary to make maximal use of the continuous operation of CHIME for pulsar observations. The transit nature of the telescope means that sources are set to be observed only when they are within 1.75° of the meridian. This results in certain parts of the sky having more sources than the number of available beams. To address this, we have developed a probabilistic scheduling algorithm that employs user-defined weights to prioritize certain sources, or positions of interest, over others. This priority system is used to resolve scheduling conflicts. There are five base weight values, where the highest weight is assigned to MSPs currently used in a PTA for gravitational-wave detection, as well as other interesting pulsars (e.g., relativistic pulsar-binary systems) such that they will be observed every day. The remaining four weighting values are defined such that each additional tier has twice the weight of the previous tier. There is also a feedback mechanism that reduces the priority associated with a source (as long as it is not assigned the highest priority level) based on the number of days it has been observed over the previous 14 days. The weight of a previously scheduled source will be reduced by a factor equivalent to the number of days observed over the period.

The scheduler adds the next source to the schedule through an iterative process. It looks for sources whose transit time began within 7 minutes of the end of the transit time of the previous source for each one of the ten beams. In cases where two or more sources fall within the time-frame, the scheduler will automatically select the source with a weight that corresponds to being observed daily and starting time of transit being closest to the end of the transit time of the previous source. If none of the sources have such weighting, each source will be given a probability equivalent to its weighting divided by the weighting of all sources in conflict and a source will be randomly selected with the determined probabilities.

In order to evaluate the effectiveness of the scheduler, we examined the number of times each source is scheduled over a 60-day period. Figure 5 shows the histograms of sources and how often they are scheduled. We found that when the telescope is not transiting the Galactic plane, the scheduler is highly effective in cycling through all sources, with more than half of the sources being observed on near-daily cadence (i.e., scheduled > 30 times over 60 days), with only about 10 of the 559 sources having a cadence of 2 weeks or more (i.e., scheduled < 4 times over 60 days). On the more crowded field of RAs between 18-20 hours, sources on average will have a longer cadence, with less than 20 sources scheduled with near-daily cadence and about

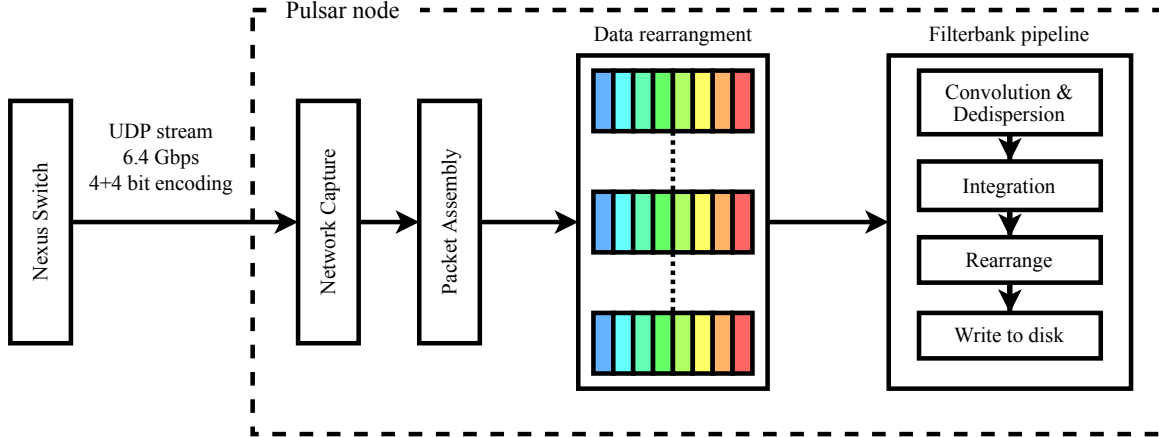


Figure 4. A schematic illustrating the various operations of the data streams from the correlator in the filterbank mode, with colors denoting frequency channels. As in the fold-mode diagram, the scrambled UDP packets from the correlator are routed to the specified pulsar node where the data are sorted and organized prior to real-time processing. However, the data stream is instead assembled into a polarization-time-frequency series and in order of increasing index variation, for reasons discussed in Section 3.3.2. The assembled data are then passed on to the coherent dedispersion pipeline process and then to filterbank generation and output.

290 out of the 620 sources having an observing cadence of 2 weeks or longer, among them 14 sources that were not scheduled at all. While this circumstance is less than ideal, it nonetheless demonstrates that the scheduler is able to cycle through most of the sources even with a large number of conflicts.

We also allow for flexibility and autonomous schedule interruption in the case of special target of opportunity events. For example, if there is a candidate alert from the CHIME/FRB system or if a radio magnetar is reported to burst, we can override the standard schedule to point at the location as soon as it is visible. It is also possible to grid around a given source position simultaneously by employing multiple tracking beams.

Multiple web-based tools are in place to actively monitor the continuous operation, including a live data-product viewer and a Grafana⁹ visualization platform for displaying system, transmission and data-storage metrics collected using the Prometheus toolkit¹⁰.

4. BACKEND PERFORMANCE

The software infrastructure and scheduling algorithm developed for the CHIME/Pulsar system, described in Section 3, allow for priority-based observations of many known pulsars in the Northern hemisphere on a continuous basis. On average, the CHIME/Pulsar system observes roughly 400–500 pulsars per day, and monitors all known sources with declinations greater than -20° at least once every ~ 4 weeks. Per-source observing cadence

varies as a function of source right ascension due to the heterogeneous nature of the pulsar sky distribution, as discussed in Section 3.4, though the CHIME/Pulsar system nonetheless observes nearly all pulsars at least once within a several-week timescale. We demonstrate the observing capabilities of the CHIME/Pulsar system by describing backend performance during the initial 1.5 years of CHIME operation (July 2018 – November 2019).

4.1. System up-time

During the “pre-commissioning” period of CHIME operations, from July 2018 to February 2019, we gradually increased the number of pulsar-backend nodes to the current ten available and employed a monthly operation cycle with a week of software deployment for new features between cycles. The CHIME/Pulsar system typically had an up-time of $\sim 70\%$ during the pre-commissioning phase of operation (including downtime due to software-deployment weeks). As expected, the on-sky observing time has increased to $\sim 100\%$ as the commissioning period continues and transitions to the “full-science” mode of CHIME operation. As of publication, the CHIME/Pulsar backend is continuously acquiring data alongside the various backends currently deployed for the CHIME telescope.

Figure 6 shows a selection of MSPs and their daily signal-to-noise ratio (S/N) variations as observed by CHIME/Pulsar backend over the year of 2019 commissioning period. These S/N variations indicate that the system is stable during the commissioning period. Some degree of S/N variation remains, though we believe this is due to imperfect excision of the time-varying RFI envi-

⁹ <https://grafana.com>

¹⁰ <https://prometheus.io>

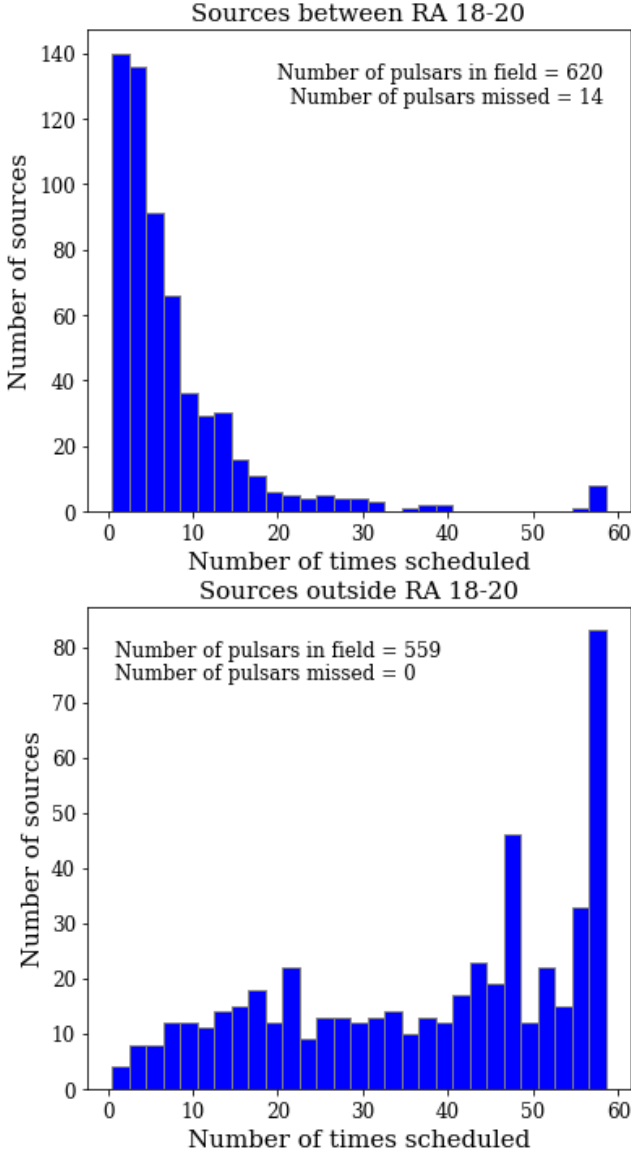


Figure 5. Histograms showing the rate that each source is observed over a period of 60 days, for sources located at Right Ascensions (RAs) of between 18-20 and for those outside of the RA range. The histograms are binned in units of two, starting with the first bar representing number of sources scheduled for either 1 or 2 times over the past 2 months. The number of sources available for each RA range and the number of sources not scheduled over the 60-day period are indicated on the plots.

ronment, imperfections in the calibration solutions, and potentially scintillation effects towards low-DM pulsars.

4.2. Radio frequency interference mitigation

Frequency channels affected by bright RFI (notably the LTE cellular network band between ~ 730 - 755 MHz and several digital television bands between 500-600 MHz) are identified from the amplitude and

phase calibration solutions provided for each antenna and frequency channel (see Section 3.1). Since these solutions are calculated and applied on a daily basis, the particular frequency channels that are masked can vary on similar timescales, but the RFI environment is generally stable.

The bulk of RFI excision occurs during post-processing (e.g., while analyzing the folded or filterbank data products). A large fraction of the corrupted data can be removed by masking an empirically constructed list of frequency channels where RFI is persistent (approximately 15% of the band). This corrupted channel mask can in principle also be combined with the calibration-based mask applied in the beamforming stage. More refined RFI excision can be attained by using techniques available in standard pulsar processing software packages, e.g., PSRCHIVE or PRESTO (Ransom 2011), but is left to user discretion. For example, in Figure 7 we have excised RFI using both the persistent corrupted channel mask and a method based on RFI cleaning utilities from the CoastGuard software suite (Lazarus et al. 2016), where several robust statistical quantities on a per channel, per subintegration basis are evaluated to determine whether samples are corrupted¹¹. Typically, we mask $\sim 25\%$ of the 1024 frequency channels, yielding ~ 300 MHz of usable bandwidth spread non-contiguously across the full 400 MHz observing band. As our understanding of the system and the RFI environment evolves, these will be tuned to improve sensitivity.

4.3. Sensitivity

CHIME is nominally capable of observing all known pulsars down to a declination of $\sim -20^\circ$. To date, we have re-detected over ~ 500 known pulsars with pre-commissioning CHIME/Pulsar observations. Out of these ~ 500 observable sources, 209 pulsars have published flux densities at 600 MHz in the *ATNF Pulsar Catalogue*¹² (Manchester et al. 2005). For these pulsars, we can compare their detected average S/N with the expected value to assess the sensitivity of the CHIME/Pulsar system.

We calculate the expected S/N for each pulsar using the radiometer equation. Many pulsars have steep spectral indices, and the sky temperature (T_{sky}) will vary significantly across the 400 MHz bandwidth. Therefore, in the estimation of the expected S/N, we separately consider three subbands and sum the three S/N values

¹¹ The exact version of the modified software used here can be found at https://github.com/bwmeiers/iterative_cleaner/tree/v0.9

¹² <http://www.atnf.csiro.au/people/pulsar/psrcat>

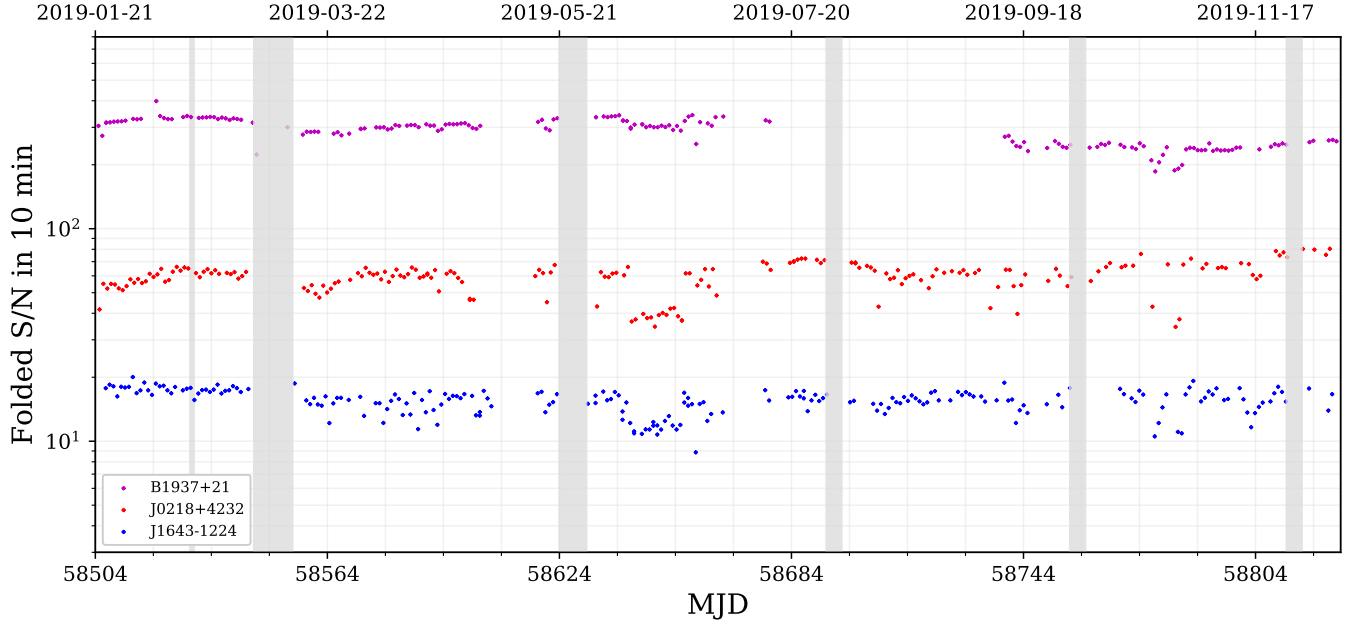


Figure 6. Observed S/N for three pulsars (PSRs J1643–1224, J0218+4232 and B1937+21) in 2019. Vertical grey bands correspond to correlator-software deployment weeks where no science-quality data were recorded.

in quadrature. We take the flux density values at 400, 600, and 800 MHz (S_{400} , S_{600} , and S_{800} respectively) from the *ATNF Pulsar Catalogue*. Where flux densities are not available, we extrapolate the subband flux density from the published spectral index. For each of the 209 sight-lines, we obtain T_{sky} at 400, 600, and 800 MHz from the Haslam survey (Haslam et al. 1982). For the system temperature (T_{sys}), we consider both the optimistic nominal value of 50 K and a pessimistic worst-case-scenario of 100 K to determine a range of expected S/N values.

Figure 8 summarizes the results of this analysis at 600 MHz. From the top left panel, it can be seen that most of our re-detections are close to the 1:1 diagonal line. The lowest published flux density of a pulsar we have re-detected is 0.6 mJy. The CHIME primary beam response is strongly dependent on frequency and zenith angle, where at large zenith angles (low declinations, blue points in Figure 8) there is a significant decrease in sensitivity. Using a preliminary model, we have taken the primary beam attenuation into account when computing the expected S/N for pulsars, equalizing the response as a function of declination.

4.4. Polarisation stability

Precision pulsar timing requires exquisite polarisation calibration. In particular, the stability of the observed polarisation properties of any given pulsar over different epochs is critical (e.g., van Straten 2006; Foster et al. 2015). A general polarisation calibration

scheme for CHIME/Pulsar is under investigation and is a high-priority item for all CHIME projects. Currently, however, we cannot transform from instrumental to intrinsic Stokes parameters. Nevertheless, Stokes profile stability can nominally be ensured by using arbitrary Mueller (transfer) matrices to effectively absorb any telescope miscalibration and depolarisation effects, including those introduced by averaging over frequency and time, when creating TOAs (e.g., Archibald et al. 2018)¹³. This approach is powerful and flexible, but it is not easy to translate the elements of the resulting transfer matrix to physical telescope properties.

To examine the stability of the Stokes parameters over time, we inspected polarisation profiles of several bright targets, including B1937+21 (see Figure 9). A high-S/N smoothed, frequency and time averaged template for each pulsar was created and used as a reference to compare observations of the same pulsar at different epochs. We compared the Stokes profiles and the resulting transfer matrix required to correct each observation to the reference profile, where the matrix elements should not differ substantially over time if the polarisation response of the system is stable. The absolute difference between the template and observed Stokes profiles (without any correction), relative to the Stokes I maximum, on different days is typically \sim 10%. Applying the arbitrary

¹³ Original code is available here: <https://github.com/aarchiba/triplesystem/> in the `template_matching.py` script.

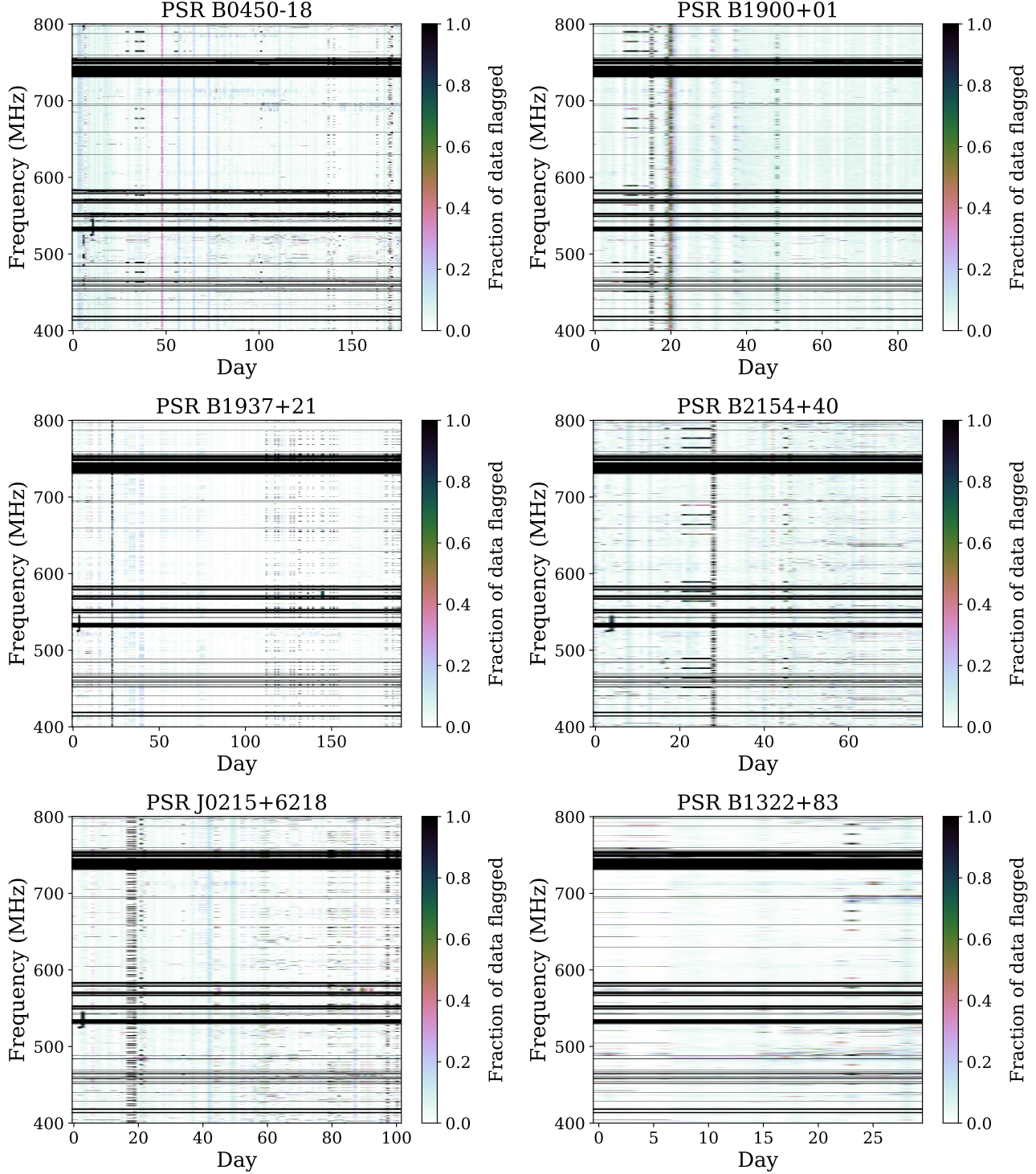


Figure 7. A sample of post-processing RFI masks over time for six pulsars covering most of the CHIME/Pulsar observable declination range. Each observation was processed identically, which included applying a mask to known bad channels and an automated process based on RFI excision routines from the *CoastGuard* software suite. The color bar represents the fraction of data flagged as RFI for each channel, for each observation. While individual observations (days) are presented in chronological order, the separation and total time spanned varies. The total time spanned for each RFI mask ranges from 164 to 324 days, and the range of observed dates is MJD 58500–58824 (2019-01-17 to 2019-12-07 UTC). The mean RFI fraction for all observations presented here is $\sim 20\%$ and the 95th percentile is $\sim 25\%$, although from day-to-day the masking fraction can vary between $\sim 15\%$ to $\sim 68\%$.

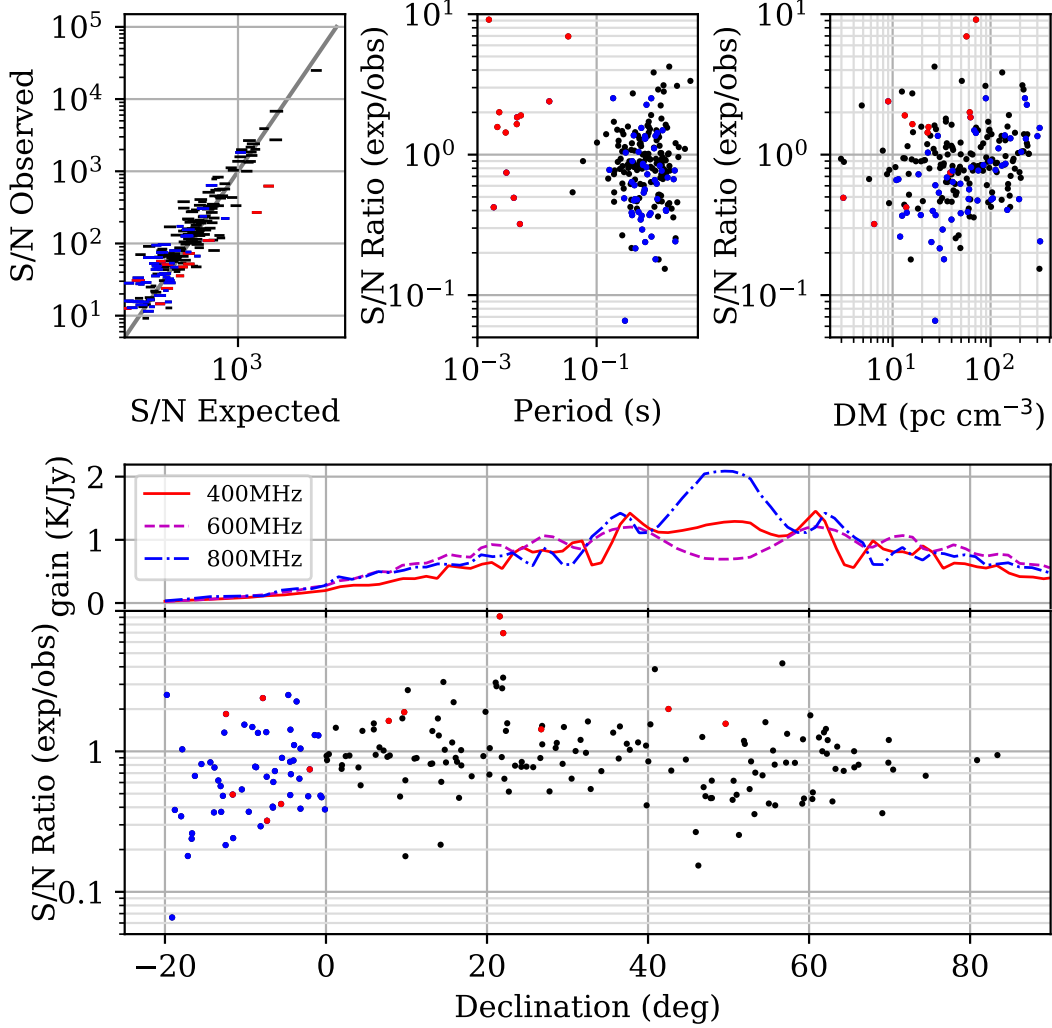


Figure 8. A study of the expected versus observed S/N for 209 pulsars with published flux densities at 600 MHz. For each pulsar, the line-of-sight T_{sky} is estimated from the Haslam sky survey. In each panel, pulsars with declination $< 0^\circ$ are highlighted in blue whereas those with short spin periods of $P < 35$ ms are highlighted in red. In the top-left panel we show the expected S/N is shown as a range for each pulsar, where the left edge of each point corresponds to a pessimistic T_{sys} of 100 K and the right edge with a T_{sys} of 50 K. The diagonal line is the 1:1 ratio, where the observed S/N equals the expected value. The ratio of the expected to observed S/N versus pulsar period (top-middle), and DM (top-right) are also shown. For simplicity, the expected S/N for each pulsar is taken to be the averaged value within the range of T_{sys} . In the lower panel, we show the ratio of the expected to observed S/N versus declination, including the nominal CHIME primary beam response correction. The beam-corrected gain as a function of declination, at 400, 600 and 800 MHz, is also provided.

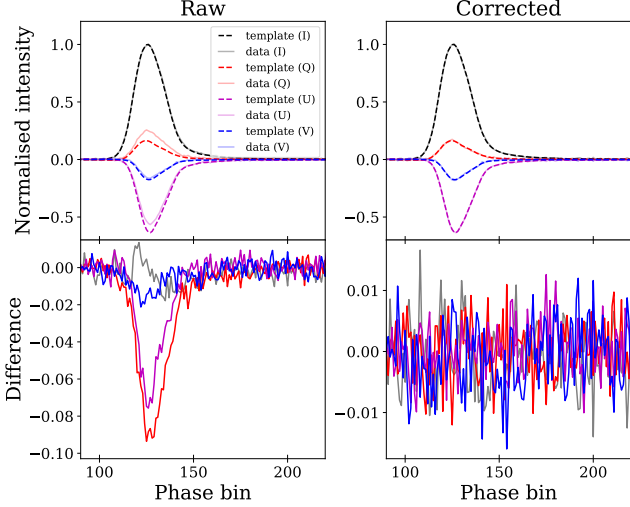


Figure 9. Comparison of the Stokes profiles from an observation of the main pulse of B1937+21 (solid lines) and a template (dashed lines). The top panels shows the uncorrected data (left) and corrected data (right) for each Stokes parameter: I (black), Q (red), U (magenta) and V (blue). The lower panels shows the residuals between the template and the raw data (left) and the corrected data (right).

inverse transfer matrix corrections results in a residual difference of $\sim 1\%$ or less. For individual pulsars, especially those which scintillate or exhibit mode changing, there are instances where the Stokes parameters change significantly on daily timescales relative to a given template.

Ultimately, polarisation stability and calibration is an on-going challenge for CHIME/Pulsar. Applying the proposed arbitrary transfer matrix approach to stabilise the Stokes parameters from day to day will be a necessary step when conducting high-precision timing data analysis. Further effort will also be made into adapting this approach to a wideband regime, where the frequency dependence of the polarisation response is also considered.

4.5. Spectral Leakage

The polyphase filterbank (PFB) used by the CHIME FX correlator applies a sinc-Hann windowing function in the Fourier domain to raw digitized sky signal when forming 1024 frequency channels across the CHIME band (Bandura et al. 2014). While chosen to maximize channel sensitivity, the imperfect response in each synthesized channel produces leakage of signal between adjacent channels. Coherent dedispersion by the CHIME/Pulsar backend will ultimately produce aliasing of the detected pulsar signal, with a frequency-dependent lag between the original pulse and its aliased counterpart across the CHIME band.

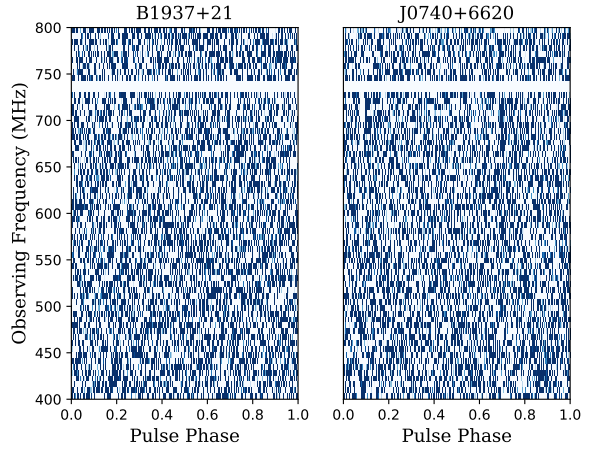


Figure 10. The presence of spectral leakage as dispersed features in CHIME/Pulsar spectra for PSRs J0740+6620 and B1937+21. In both panels, pulse profiles were removed using a principal component analysis for determining de-noised representations of the on-pulse dynamic spectrum. The spectrum for B1937+21 was obtained after integrating a single (~ 10 -min) fold-mode recording, whereas the spectrum for J0740+6620 was determined by coherently averaging over 100 individual epochs of ~ 20 -min recordings. Vertical artifacts arise due to imperfect estimation of the de-noised template profiles.

Figure 10 shows examples of spectral leakage in pulse-averaged spectra for PSRs B1937+21 and J0740+6620. Artifacts due to leakage are apparent within a single observation of PSR B1937+21 with CHIME/Pulsar, though similar features are far less prominent in slower, fainter pulsars like J0740+6620, even after integrating data taken over 100 epochs as shown in Figure 10.

The MeerTime pulsar-timing backend mitigates spectral leakage in the MeerKAT observing system by using a modified sinc-Hann windowing function in their F-engine system; the modified windowing function used by MeerTime suppresses the response of the synthesized-channel boundaries, which minimizes leakage but simultaneously lowers effective sensitivity in each channel (Bailes et al. 2016). The commensal nature of pulsar/FRB observations with CHIME requires that the F-engine use the same PFB configuration for all backends when generating channelized data streams. Therefore, spectral leakage will be present to varying degrees in CHIME/Pulsar observations and its impact on timing will be assessed during offline processing.

4.6. Timing

In order to establish the timing capabilities of the CHIME/Pulsar system, we collected near-daily observations of MSPs observed by the North American Nanohertz Observatory for Gravitational Waves

(NANOGrav) during a several-month commissioning period when telescope sensitivity was generally stable. We used timing solutions for online folding that are also used by NANOGrav at the 305-m Arecibo Observatory and the 100-m Green Bank Telescope (GBT) for pulsar-timing data acquisition. Initial “template” pulse profiles of CHIME/Pulsar data, necessary for cross-correlation and arrival-time estimation, were generated by excising channels containing RFI, coherently adding timing data taken across the commissioning period, and fully averaging the stacked set in time and frequency. The time- and frequency-averaged profile was then de-noised using a wavelet transform.

Times of arrival (TOAs) were then computed via cross-correlation between the template profiles and a downsampled form of the CHIME/Pulsar fold-mode timing data. For analysis of NANOGrav pulsars, we fully integrated available fold-mode data in time and downsampled in frequency from the native resolution to 32 channels prior to TOA generation, yielding a maximum of 32 channelized TOAs per epoch. This level of downsampling is similar to the reduction methods used by NANOGrav in order to evaluate DM variations over time (e.g. Levin et al. 2016).

Best-fit timing residuals for PSR J0645+5158, computed using the TEMPO pulsar-timing analysis package¹⁴ (Nice et al. 2015) when modeling NANOGrav and CHIME/Pulsar TOA data simultaneously, are shown in Figure 11. We used the timing solution generated for the 12.5-yr NANOGrav data release (Alam et al. 2021a,b) to model this combined data set, fitting for physical and instrumental parameters such as: pulsar-spin frequency and its first time derivative; astrometry (ecliptic coordinates, proper motion, and timing parallax); DM values estimated within one-day bins; and an arbitrary offset between the NANOGrav and CHIME data that reflects instrumental differences. As shown in Figure 11, we found that a numerically adequate timing model can be achieved when combining the CHIME and NANOGrav data sets, yielding best-fit parameters and fit statistics consistent with those previously reported from NANOGrav. The RMS residual for the CHIME data set on J0645+5158 is 0.83 μ s, which compares well with the RMS values for the GBT data sets collected using the 800-MHz receiver (0.71 μ s) and 1400-MHz receiver (1.38 μ s). A detailed timing study of NANOGrav sources observed with CHIME will be presented in a forthcoming study.

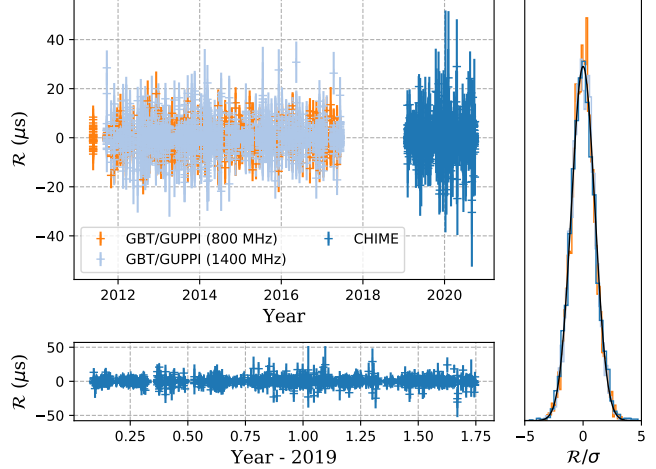


Figure 11. A summary of best-fit timing residuals (\mathcal{R}) for PSR J0645+5158. *Top-left*. The orange and light-blue points denote TOAs and best-fit estimates of \mathcal{R} collected with the GBT using the 800-MHz and 1400-MHz receivers, respectively, as part of the NANOGrav 12.5-yr data release. Dark-blue points are TOAs and best-fit \mathcal{R} measured from CHIME/Pulsar data. *Bottom-left*. A zoomed-in view of the CHIME/Pulsar timing data. *Right*. Normalized distributions of \mathcal{R} weighted by σ , shown for all three TOA subsets as stepped histograms. The black line shows a unit-normal distribution for comparison, indicating that the CHIME/Pulsar system yields timing data with expected statistical properties and are consistent with TOAs obtained using other observatories.

5. SCIENTIFIC MOTIVATION

As described above, CHIME/Pulsar is a flexible system with a variety of acquisition modes that is designed for continuous and autonomous operation. Here we briefly outline some of the major scientific cases that will be explored by the CHIME/Pulsar project.

5.1. Long-term Timing

The long-term timing of pulsars, with a focus on PTA targets, is the primary science driver for CHIME/Pulsar. Detection of nanohertz-frequency gravitational waves using a PTA directly depends on a regular, high-cadence observing program of a large MSP sample over many years. The CHIME/Pulsar system is naturally producing such a data set with near-daily cadence. As such, CHIME/Pulsar timing data of NANOGrav sources (e.g. Arzoumanian et al. 2018) will be combined in future NANOGrav data releases in order to improve detection of the stochastic GW background at nanohertz frequencies.

The autonomous design of the CHIME/Pulsar system, combined with the wide field of view of the telescope, allows for regular, priority-based timing observations of sufficiently bright pulsars, with 400–500 pulsars signifi-

¹⁴ <https://sourceforge.net/projects/tempo>

cantly detected within a single day of operation. This capability is unprecedented in the northern hemisphere and only recently achieved for southern pulsars with the development of the MeerKAT pulsar timing program (MeerTime; Bailes et al. 2016) and the UTMOST pulsar instrument (Bailes et al. 2017; Jankowski et al. 2019). The CHIME/Pulsar system actively monitors observable sources that are reported in the ATNF pulsar catalogue with a range of cadence. CHIME/Pulsar also observes newly discovered pulsars found by the Green Bank North Celestial Cap (GBNCC; Stovall et al. 2014) survey in order to aid in the confirmation and follow-up of their discovered sources.

5.2. High-cadence Timing of Pulsar-Binary Systems

Long-term timing of binary radio pulsars often yields secular and/or periodic variations from purely Keplerian motion. The most famous examples of secular variations are those associated with general-relativistic orbital decay and precession in compact orbits (see Stairs 2003, for a review), though many non-relativistic pulsar orbits have been observed to vary over time due to evolving sky orientations induced by proper motion (e.g. Kopeikin 1995, 1996). By contrast, the relativistic Shapiro time delay (Shapiro 1964) is a periodic effect observed in sufficiently inclined binary systems of any size where the pulsed signal traverses varying amount of spacetime curvature induced by the companion star over the course of the orbit. Measurements of such effects allow for direct constraints on the masses (e.g., PSR J0740+6622; Cromartie et al. 2020) and geometry of the systems in question (e.g., PSR J0437–4715; van Straten et al. 2001), and thus stand to yield high-impact information that is otherwise inaccessible from purely Keplerian dynamics.

The CHIME/Pulsar system is expected to produce a rich data set for probing binary astrophysics by monitoring all visible binary pulsars with near-daily observing cadences over the course of telescope operation. As an example, Figure 12 shows simulated best-fit estimates of a timing parameter quantifying relativistic time dilation and gravitational redshift in the PSR J0509+3801 double-neutron-star system (Lynch et al. 2018). While typical programs observe such sources on monthly or bi-monthly cadences, the simulated estimates in Figure 12 suggest that such effects can be better constrained with high-cadence observations – like those achievable with CHIME/Pulsar – due to quickened evaluations of orbital parameters and their variations. Moreover, we anticipate the daily cadence to yield detections of the Shapiro delay on timescales much shorter than those typically seen in current pulsar-timing literature, due to the faster rate of achieving dense orbital coverage.

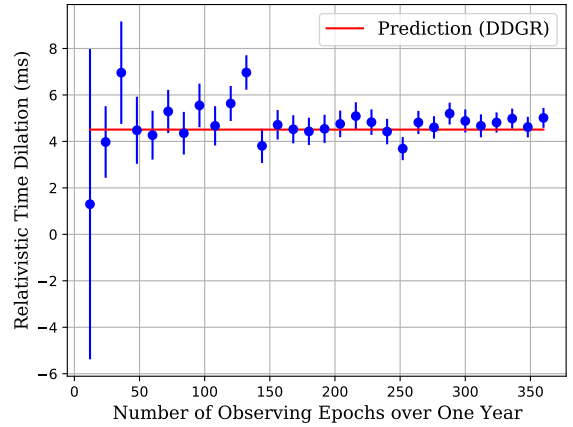


Figure 12. Estimates of the relativistic parameter quantifying time dilation and gravitational redshift for PSR J0509+3801 – typically referred to as γ in pulsar-timing literature – derived from simulated TOA data sets with TOAs collected over one year in time but with different observing cadences. For each plotted measurement, a timing data set is generated with `tempo` assuming that one frequency/time-averaged TOA is obtained per epoch, and that the TOA data set yields white-noise properties consistent with current CHIME/Pulsar observations of J0509+3801 (i.e., epoch-averaged RMS residual of $\sim 70 \mu\text{s}$). The red horizontal line marks the expected value determined by Lynch et al. (2018) when modeling their TOAs using the “DDGR” timing model, that assumes all variations are effects predicted by general relativity.

5.3. Plasma propagation effects

Pulsars are sensitive probes of the ISM and its structural variations across many lines of sight. By processing and recording data at low radio frequencies, the CHIME/Pulsar system is producing a rich and growing data set for autonomously monitoring frequency-dependent features in pulsar data. Examples of such effects include temporal variation of DM (e.g. Lam et al. 2016; Lentati et al. 2017; Lam et al. 2018), frequency-dependent DM (Cordes et al. 2016; Donner et al. 2019), “echoes” in pulsar spectra (e.g. Graham Smith et al. 2011; Michilli et al. 2018; Driessen et al. 2019; Bansal et al. 2020), “extreme scattering events” in flux density modulations (e.g. Coles et al. 2015; Kerr et al. 2018), scintillation (e.g. Bhat et al. 1999b,a,c; Wang et al. 2005, 2008) or multi-path scattering/pulse broadening (e.g. Bhat et al. 2004; McKee et al. 2018) caused by small-scale plasma structures. Understanding these effects is critical in achieving a GW background detection using PTAs (e.g. Cordes & Shannon 2010; Levin et al. 2016), but are also informative when considering pulsar

astrometry and system dynamics (e.g. Lyne 1984; Pen et al. 2014; Reardon et al. 2019).

As a demonstration of the suitability of CHIME/Pulsar for studying small-scale dispersive variations, we measured the DM time series for PSR B1937+21, one of the fastest-known MSPs, and one that is known to exhibit large and rapid variations in DM (e.g. Jones et al. 2017), following the process detailed in Donner et al. (2019). The 10 highest-S/N observations were selected, which were phase-aligned and summed to create a high-S/N frequency-resolved reference profile, with very little correlated noise. The original 1024 frequency channels were integrated to 16 channels, and a wavelet smoothing algorithm was applied, resulting in a noise-free standard template. The remaining observations in our data set were also integrated to 16 frequency channels, and TOAs were measured for each via cross-correlation with the template. The TOAs were analysed using TEMPO2¹⁵ (Hobbs et al. 2006), with a timing model based on the one presented in Perera et al. (2019), with the time-varying DM and noise models removed. We fit for DM on each observing epoch while keeping the other timing-model parameters fixed to obtain a time series with a mean cadence of 1.2 days and a median DM precision of $2.9 \times 10^{-5} \text{ pc cm}^{-3}$, which we present in Figure 13. As a comparison, the DM time series for B1937+21 obtained from NANOGrav observations with the Arecibo and Green Bank observatories yield a similar mean DM precision of $\sim 2 \times 10^{-5} \text{ pc cm}^{-3}$, though evaluated over a monthly cadence Alam et al. (2021a,b). The measured DM time series from CHIME/Pulsar data displays an overall linear trend, with additional short-duration excesses lasting a few tens of days, which would not be easily-resolved in low-cadence data sets (such as those normally employed by PTA experiments).

Another important PTA science consideration that will benefit from the CHIME/Pulsar observing campaign is the study of the Solar wind, which contributes an annual variation in DM to pulsar timing data. This effect varies in time, throughout the course of the 11-yr Solar cycle, and it has been proposed (e.g. Madison et al. 2019, Tiburzi et al. 2019) that long-term, high-cadence radio monitoring of pulsars close to the ecliptic plane will provide valuable information about this phenomenon. Recent work has shown that in high-cadence data sets with high DM precision, typical simple Solar wind models do not adequately-describe the excess dispersive delay (Tiburzi et al. 2019), and that its ro-

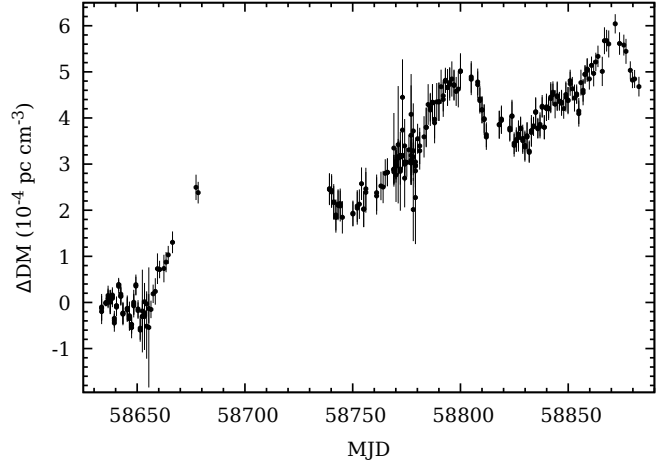


Figure 13. DM time series measured from CHIME observations of PSR B1937+21, relative to the initial value of $71.01572 \text{ pc cm}^{-3}$. Each observation was integrated in frequency to 16 channels, with a TOA measured per channel. The DM was determined by fitting for the frequency-dependent dispersive delay between in-band TOAs for each day. The median DM uncertainty is $2.9 \times 10^{-5} \text{ pc cm}^{-3}$. The mean cadence following MJD 58742 is 1.2 days.

bust mitigation will become increasingly important in searches for low-frequency gravitational waves as pulsar timing array sensitivity continues to improve (Madison et al. 2019).

5.4. Polarization

Polarization properties of radio pulsars have provided a wealth of information about their emission mechanism and geometry, and about the magnetised Galactic medium (e.g. Lorimer & Kramer 2004). The CHIME/Pulsar backend records and stores full Stokes information, allowing polarization studies to be performed for all detected sources. However, polarization calibration, necessary for many pulsar studies, is difficult to obtain for a transit telescope such as CHIME, where the interplay between the two orthogonal sets of feeds changes during the observation and is strongly frequency dependent. Obtaining a beam model of the telescope accurate enough to recover the intrinsic polarization of the signal is a work in progress involving measurements from various CHIME backends, including CHIME/Pulsar (see also Section 4.4). Nevertheless, even before being able to calibrate the instrument, some interesting properties of polarized sources can be measured, and in particular the effect of Faraday rotation. CHIME/Pulsar, operating at low frequencies and with a large fractional bandwidth, is able to provide very precise measurements of rotation measure (RM).

The capability of CHIME/Pulsar to measure precise RM values has already been demonstrated in a recent

¹⁵ <https://bitbucket.org/psrsoft/tempo2/src/master>

work by Ng et al. (2020a), where we present RM values for 80 pulsars, 55 of which are measured for the first time. We plan to measure the RM of most detectable northern pulsars, many of which either do not have a reported RM value, or the catalogued value was measured decades ago. By virtue of observing a large fraction of northern pulsars regularly, CHIME/Pulsar will also significantly contribute to efforts to map the Galactic magnetic field, complementing similar ongoing studies at low frequencies (e.g. Lenc et al. 2018; Sobey et al. 2019). In addition, frequent observations present an exciting opportunity to investigate temporal RM variations of every observed source. Measuring simultaneous DM variations, as described in §5.3, will enable the measurement of Galactic magnetic field gradient.

5.5. Glitch monitoring

Approximately 200 pulsars to date¹⁶ have been observed to exhibit “glitches”, where their rotation period abruptly changes and can remain altered for several weeks or months subsequently (e.g. Radhakrishnan & Manchester 1969; Weltevrede et al. 2011; McKee et al. 2016; Lower et al. 2020). Studying glitches and their aftermath provides insight into the interior structure of neutron stars and the nuclear equation of state (e.g. Haskell & Melatos 2015; Haskell & Sedrakian 2018). The modular design of the CHIME/Pulsar system lends itself to immediate, offline analysis of timing variations consistent with pulsar glitches from many different sources, and potentially enables near-realtime alerting of such events to the transient-astronomical community. Such analyses are especially interesting in the era of LIGO/VIRGO detection of GWs, where correlations of glitch and GW transient events are expected to yield multi-messenger constraints on the interior structure of neutron stars. Furthermore, the observing cadence of the pulsar with a detected glitch can be increased in order to better model the post-glitch recovery properties of the pulsar.

5.6. Monitoring for emission variability in pulsating sources

Daily observations, flexible recording configurations, and a wide observing band are ideal for long-term monitoring of the emission from objects such as repeating FRBs (e.g. Spitler et al. 2016; CHIME/FRB Collaboration et al. 2019a,b; Fonseca et al. 2020), RRATs (McLaughlin et al. 2006), intermittent (Kramer et al.

2006), nulling (Backer 1970a), and mode-changing pulsars (Backer 1970b; Lyne 1971; Naidu et al. 2017). This will allow us to probe any short and long-term variation in the rotational properties of the sources and their potential link with the variability in emission properties (e.g. Lyne et al. 2010; Perera et al. 2016; Stairs et al. 2019; Naidu et al. 2018).

The high-cadence observations also allow us to search for previously unknown emission variability in known pulsars. As a testament to this, Ng et al. (2020b) identified new nulling and mode changing pulsars from the commissioning data set (July 2018 to March 2019).

5.7. Searching for pulsars, RRATs, pulses from repeating FRBs and transient astronomical events

The filterbank mode of the CHIME/Pulsar backend is being actively used to follow up both unknown single pulses of Galactic origin (Good et al., submitted) and repeating FRB sources discovered by CHIME/FRB. The large instantaneous field of view and the transit nature of CHIME/FRB has allowed for the blind detection of these sources. A number of these sources are then followed up with the more sensitive CHIME/Pulsar backend as the data are coherently dedispersed to the DM of the sources, allowing detection of faint pulses that will otherwise be missed by CHIME/FRB. Moreover, the tracking beams generated for CHIME/Pulsar remain centered on the positions of the sources during their transit at the CHIME site, allowing for robust detection of the intrinsic dynamic spectrum. Furthermore, CHIME/Pulsar has a time resolution of 327.68 μs, three times higher than CHIME/FRB, that could resolve smaller scale structures of the single pulses otherwise undetectable by CHIME/FRB.

Follow-up tracking observations of the unknown Galactic sources with CHIME/Pulsar is also used to look for periodicity akin to pulsars and RRATs. These are done by either measuring the gaps between successive pulses, or periodicity searches including both Fast Fourier Transform and “fast folding algorithms” (e.g. Parent et al. 2018). The new candidates detected by the CHIME/FRB system and confirmed by CHIME/Pulsar are subsequently monitored for long-term timing¹⁷. New Galactic discoveries from the use of both CHIME/FRB and CHIME/Pulsar is reported in Good et al. (2020).

While individual observations of a source with CHIME/Pulsar are limited by the primary beam size of CHIME which restricts transit time, the capability to perform multiple simultaneous observations means that

¹⁶ See <http://www.jb.man.ac.uk/pulsar/glitches/gTable.html> and <http://www.atnf.csiro.au/research/pulsar/psrcat/glitchTbl.html> for a list of glitches and their corresponding publications.

¹⁷ See <https://www.chime-frb.ca/galactic>

we can afford to repeatedly observe a number of sources daily to stack and search the data for pulsations. This will allow for the potential detection of faint sources by leveraging long integration times. Such strategy has been employed before in targeted searches of globular clusters (e.g. Cadelano et al. 2018).

CHIME/Pulsar is also able to rapidly follow up on any transient astronomical events that might emit radio pulses. The regular schedule can be overwritten quickly to point a pulsar beam towards the source of interest during the forthcoming transit. We expect to apply the capability to follow up on events such as magnetars undergoing X-ray outburst (e.g. Camilo et al. 2006; Rea et al. 2013; Esposito et al. 2020), gravitational wave events (Abbott et al. 2016, 2017) and new transitional MSPs (Archibald et al. 2009).

As with fold-mode observations, filterbank scans of known or candidate sources are assigned priorities and included in the automatic scheduling of acquisition with CHIME/Pulsar. However, it is possible to instead program CHIME/Pulsar to operate as a dedicated blind-search machine. In this case, the FX correlator and CHIME/Pulsar backend can beamform and process, respectively, up to \sim 3000 distinct lines of sight per day for 5-minute acquisition times.

6. CONCLUSIONS & FUTURE DIRECTIONS

In this work, we reported on a system built for the CHIME telescope to enable radio pulsar observations in different modes of acquisition. We described the hardware setup of the CHIME/Pulsar backend and provided details on the software/networking modules that were developed to interact with the CHIME FX-correlator for generating 10 synthesized tracking beams based on autonomous source selection and scheduling. The CHIME/Pulsar system operates in tandem with the cosmology and FRB experiments, and is capable of regularly recording data in both “fold” and filterbank modes of pulsar observations. The CHIME/Pulsar system is poised to make a wide variety of important science contributions ranging from detailed studies of known sources and discoveries of new ones, to investigations of the ISM, both on its own and in collaboration with other instruments.

ACKNOWLEDGMENTS

We are grateful to the staff of the Dominion Radio Astrophysical Observatory, which is operated by the National Research Council of Canada. CHIME is funded by a grant from the Canada Foundation for Innovation (CFI) 2012 Leading Edge Fund (Project 31170) and by contributions from the provinces of British Columbia, Québec and Ontario. The CHIME/FRB Project, which enabled development in common with the CHIME/Pulsar instrument, is funded by a grant from the CFI 2015 Innovation Fund (Project 33213) and by contributions from the provinces of British Columbia and Québec, and by the Dunlap Institute for Astronomy and Astrophysics at the University of Toronto. Additional support was provided by the Canadian Institute for Advanced Research (CIFAR), McGill University and the McGill Space Institute thanks to the Trottier Family Foundation, and the University of British Columbia. The CHIME/Pulsar instrument hardware was funded by NSERC RTI-1 grant EQPEQ 458893-2014. We thank Erik C. Madsen for his work in planning the development of the CHIME/Pulsar backend. We also thank the anonymous referee for their feedback and suggestions, which improved the quality of this work. Pulsar research at UBC is funded by a NSERC Discovery Grant and by CIFAR. This research was enabled in part by support provided by WestGrid (www.westgrid.ca) and Compute Canada (www.computecanada.ca). V.M.K. holds the Lorne Trottier Chair in Astrophysics & Cosmology and a Distinguished James McGill Professorship and receives support from an NSERC Discovery Grant and Herzberg Award, from an R. Howard Webster Foundation Fellowship from the CIFAR, and from the FRQNT Centre de Recherche en Astrophysique du Québec. D.M. is a Banting Fellow. S.M.R. is a CIFAR Fellow and is supported by the National Science Foundation (NSF) Physics Frontiers Center award 1430284. The National Radio Astronomy Observatory is a facility of the NSF operated under cooperative agreement by Associated Universities, Inc. P.S. is a Dunlap Fellow and an NSERC Postdoctoral Fellow. The Dunlap Institute is funded through an endowment established by the David Dunlap family and the University of Toronto. C.L. was supported by the U.S. Department of Defense (DoD) through the National Defense Science & Engineering Graduate Fellowship (NDSEG) Program. M.D. receives support from a Killam fellowship, NSERC Discovery Grant, CIFAR, and from the FRQNT Centre de Recherche en Astrophysique du Québec.

Software: DSPSR (van Straten & Bailes 2011), PSR-DADA (<http://psrdada.sourceforge.net>), PSRCHIVE (Hotan et al. 2004; van Straten et al. 2012), PRESTO (Ransom 2011), TEMPO (Nice et al. 2015), TEMPO2 (Hobbs et al. 2006)

Table 3. The first 15 rows from the machine-readable table of observed sources.

(1) PSR	(2) Start MJD	(3) Number of obs. per week ^a	(4) Mean S/N ^{a,b}
J0002+6216	59033	2.8	4
J0006+1834	58441	6.4	12
J0011+08	59031	5.9	11
B0011+47	58170	6.3	129
J0023+0923	58440	6.6	23
J0026+6320	58441	6.3	67
J0030+0451	58443	5.8	37
J0033+57	58413	6.6	4
J0033+61	59179	6.3	13
J0034-0534	58439	5.3	15
B0031-07	58170	4.7	118
J0034+69	59030	7.0	4
J0039+35	59032	3.7	5
B0037+56	58170	5.6	189
B0045+33	58170	2.8	78

^aMean values were calculated over a representative 3-month period.

^bS/N values for each observation were computed after integrating over transit time and observing frequency.

APPENDIX

A. OBSERVED PULSAR LIST

We collected observing statistics for all pulsars from the ATNF Pulsar Catalogue over a representative time period, MJD 59100–59274, where the scheduling algorithm described in Section 3.4 was executed with no modifications. This information is provided in the accompanying machine-readable table, and a small example is given in Table 3. The table columns are described as follows:

Column 1 (psr_name): The pulsar name.

Column 2 (start_mjd): The MJD corresponding to the first observation of the pulsar with CHIME/Pulsar.

Column 3 (avg_obs_per_week): The mean number of observations per week for the pulsar.

Column 4 (avg_snr_per_obs): The mean time- and frequency-averaged S/N for a typical observations of the pulsar.

REFERENCES

- Abbott, B. P., Abbott, R., Abbott, T. D., et al. 2016,
ApJL, 826, L13, doi: [10.3847/2041-8205/826/1/L13](https://doi.org/10.3847/2041-8205/826/1/L13)
- . 2017, ApJL, 848, L12, doi: [10.3847/2041-8213/aa91c9](https://doi.org/10.3847/2041-8213/aa91c9)
- Alam, M. F., Arzoumanian, Z., Baker, P. T., et al. 2021a,
ApJS, 252, 4, doi: [10.3847/1538-4365/abc6a0](https://doi.org/10.3847/1538-4365/abc6a0)
- . 2021b, ApJS, 252, 5, doi: [10.3847/1538-4365/abc6a1](https://doi.org/10.3847/1538-4365/abc6a1)
- Antoniadis, J. 2021, MNRAS, 501, 1116,
doi: [10.1093/mnras/staa3595](https://doi.org/10.1093/mnras/staa3595)
- Archibald, A. M., Stairs, I. H., Ransom, S. M., et al. 2009,
Science, 324, 1411, doi: [10.1126/science.1172740](https://doi.org/10.1126/science.1172740)
- Archibald, A. M., Gusinskaia, N. V., Hessels, J. W. T.,
et al. 2018, Nature, 559, 73,
doi: [10.1038/s41586-018-0265-1](https://doi.org/10.1038/s41586-018-0265-1)

- Arzoumanian, Z., Brazier, A., Burke-Spolaor, S., et al. 2018, ApJS, 235, 37, doi: [10.3847/1538-4365/aab5b0](https://doi.org/10.3847/1538-4365/aab5b0)
- Backer, D. C. 1970a, Nature, 228, 42, doi: [10.1038/228042a0](https://doi.org/10.1038/228042a0)
- . 1970b, Nature, 228, 1297, doi: [10.1038/2281297a0](https://doi.org/10.1038/2281297a0)
- Bailes, M., Barr, E., Bhat, N. D. R., et al. 2016, in 2016mks conf, 11. <https://arxiv.org/abs/1803.07424>
- Bailes, M., Jameson, A., Flynn, C., et al. 2017, PASA, 34, e045, doi: [10.1017/pasa.2017.39](https://doi.org/10.1017/pasa.2017.39)
- Bandura, K., Addison, G. E., Amiri, M., et al. 2014, Canadian Hydrogen Intensity Mapping Experiment (CHIME) pathfinder, Vol. 9145, 914522, doi: [10.1111/12.2054950](https://doi.org/10.1111/12.2054950)
- Bandura, K., Bender, A. N., Cliche, J. F., et al. 2016, Journal of Astronomical Instrumentation, 5, 1641005, doi: [10.1142/S2251171716410051](https://doi.org/10.1142/S2251171716410051)
- Bansal, K., Taylor, G. B., Stovall, K., & Dowell, J. 2020, ApJ, 892, 26, doi: [10.3847/1538-4357/ab76bc](https://doi.org/10.3847/1538-4357/ab76bc)
- Bassa, C. G., Janssen, G. H., Stappers, B. W., et al. 2016, MNRAS, 460, 2207, doi: [10.1093/mnras/stw1134](https://doi.org/10.1093/mnras/stw1134)
- Bhat, N. D. R., Cordes, J. M., Camilo, F., Nice, D. J., & Lorimer, D. R. 2004, ApJ, 605, 759, doi: [10.1086/382680](https://doi.org/10.1086/382680)
- Bhat, N. D. R., Gupta, Y., & Rao, A. P. 1999a, ApJ, 514, 249, doi: [10.1086/306919](https://doi.org/10.1086/306919)
- Bhat, N. D. R., Rao, A. P., & Gupta, Y. 1999b, ApJS, 121, 483, doi: [10.1086/313198](https://doi.org/10.1086/313198)
- . 1999c, ApJ, 514, 272, doi: [10.1086/306920](https://doi.org/10.1086/306920)
- Cadelano, M., Ransom, S. M., Freire, P. C. C., et al. 2018, ApJ, 855, 125, doi: [10.3847/1538-4357/aaac2a](https://doi.org/10.3847/1538-4357/aaac2a)
- Camilo, F., Ransom, S. M., Halpern, J. P., et al. 2006, Nature, 442, 892, doi: [10.1038/nature04986](https://doi.org/10.1038/nature04986)
- CHIME/FRB Collaboration, Amiri, M., Bandura, K., et al. 2018, ApJ, 863, 48, doi: [10.3847/1538-4357/aad188](https://doi.org/10.3847/1538-4357/aad188)
- . 2019a, Nature, 566, 235, doi: [10.1038/s41586-018-0864-x](https://doi.org/10.1038/s41586-018-0864-x)
- CHIME/FRB Collaboration, Andersen, B. C., Bandura, K., et al. 2019b, ApJL, 885, L24, doi: [10.3847/2041-8213/ab4a80](https://doi.org/10.3847/2041-8213/ab4a80)
- Christy, B., Anella, R., Lommen, A., et al. 2014, ApJ, 794, 163, doi: [10.1088/0004-637X/794/2/163](https://doi.org/10.1088/0004-637X/794/2/163)
- Coles, W. A., Kerr, M., Shannon, R. M., et al. 2015, ApJ, 808, 113, doi: [10.1088/0004-637X/808/2/113](https://doi.org/10.1088/0004-637X/808/2/113)
- Cordes, J. M., & Shannon, R. M. 2010, to be submitted to ApJ, arXiv:1010.3785. <https://arxiv.org/abs/1010.3785>
- Cordes, J. M., Shannon, R. M., & Stinebring, D. R. 2016, ApJ, 817, 16, doi: [10.3847/0004-637X/817/1/16](https://doi.org/10.3847/0004-637X/817/1/16)
- Cromartie, H. T., Fonseca, E., Ransom, S. M., et al. 2020, NatAs, 4, 72, doi: [10.1038/s41550-019-0880-2](https://doi.org/10.1038/s41550-019-0880-2)
- Demorest, P. B., Pennucci, T., Ransom, S. M., Roberts, M. S. E., & Hessels, J. W. T. 2010, Nature, 467, 1081, doi: [10.1038/nature09466](https://doi.org/10.1038/nature09466)
- Deng, M., & Campbell-Wilson, D. 2014, in 16th International Symposium on Antenna Technology and Applied Electromagnetics (ANTEM) (IEEE), 1–2, doi: [10.1109/ANTEM.2014.6887670](https://doi.org/10.1109/ANTEM.2014.6887670)
- Denman, N., Renard, A., Vanderlinde, K., et al. 2020, JAI, 9, 2050014, doi: [10.1142/S2251171720500142](https://doi.org/10.1142/S2251171720500142)
- Donner, J. Y., Verbiest, J. P. W., Tiburzi, C., et al. 2019, A&A, 624, A22, doi: [10.1051/0004-6361/201834059](https://doi.org/10.1051/0004-6361/201834059)
- Driessen, L. N., Janssen, G. H., Bassa, C. G., Stappers, B. W., & Stinebring, D. R. 2019, MNRAS, 483, 1224, doi: [10.1093/mnras/sty3192](https://doi.org/10.1093/mnras/sty3192)
- Espinosa, C. M., Lyne, A. G., Stappers, B. W., & Kramer, M. 2011, MNRAS, 414, 1679, doi: [10.1111/j.1365-2966.2011.18503.x](https://doi.org/10.1111/j.1365-2966.2011.18503.x)
- Esposito, P., Rea, N., Borghese, A., et al. 2020, ApJL, 896, L30, doi: [10.3847/2041-8213/ab9742](https://doi.org/10.3847/2041-8213/ab9742)
- Fonseca, E., Andersen, B. C., Bhardwaj, M., et al. 2020, ApJL, 891, L6, doi: [10.3847/2041-8213/ab7208](https://doi.org/10.3847/2041-8213/ab7208)
- Foster, G., Karastergiou, A., Paulin, R., et al. 2015, MNRAS, 453, 1489, doi: [10.1093/mnras/stv1722](https://doi.org/10.1093/mnras/stv1722)
- Good, D. C., Andersen, B. C., Chawla, P., et al. 2020, submitted to ApJ, arXiv:2012.02320. <https://arxiv.org/abs/2012.02320>
- Graham Smith, F., Lyne, A. G., & Jordan, C. 2011, MNRAS, 410, 499, doi: [10.1111/j.1365-2966.2010.17459.x](https://doi.org/10.1111/j.1365-2966.2010.17459.x)
- Haskell, B., & Melatos, A. 2015, IJMD, 24, 1530008, doi: [10.1142/S0218271815300086](https://doi.org/10.1142/S0218271815300086)
- Haskell, B., & Sedrakian, A. 2018, Astrophysics and Space Science Library, Vol. 457, Superfluidity and Superconductivity in Neutron Stars (NewCompStar), 401, doi: [10.1007/978-3-319-97616-7_8](https://doi.org/10.1007/978-3-319-97616-7_8)
- Haslam, C. G. T., Salter, C. J., Stoffel, H., & Wilson, W. E. 1982, A&AS, 47, 1
- Hobbs, G. B., Edwards, R. T., & Manchester, R. N. 2006, MNRAS, 369, 655, doi: [10.1111/j.1365-2966.2006.10302.x](https://doi.org/10.1111/j.1365-2966.2006.10302.x)
- Hotan, A. W., van Straten, W., & Manchester, R. N. 2004, PASA, 21, 302, doi: [10.1071/AS04022](https://doi.org/10.1071/AS04022)
- Jankowski, F., Bailes, M., van Straten, W., et al. 2019, MNRAS, 484, 3691, doi: [10.1093/mnras/sty3390](https://doi.org/10.1093/mnras/sty3390)
- Jones, M. L., McLaughlin, M. A., Lam, M. T., et al. 2017, ApJ, 841, 125, doi: [10.3847/1538-4357/aa73df](https://doi.org/10.3847/1538-4357/aa73df)
- Kaplan, D. L., Kupfer, T., Nice, D. J., et al. 2016, ApJ, 826, 86, doi: [10.3847/0004-637X/826/1/86](https://doi.org/10.3847/0004-637X/826/1/86)
- Karuppusamy, R., Stappers, B. W., & Lee, K. J. 2012, A&A, 538, A7, doi: [10.1051/0004-6361/201117667](https://doi.org/10.1051/0004-6361/201117667)
- Kerr, M., Coles, W. A., Ward, C. A., et al. 2018, MNRAS, 474, 4637, doi: [10.1093/mnras/stx3101](https://doi.org/10.1093/mnras/stx3101)
- Kopeikin, S. M. 1995, ApJL, 439, L5, doi: [10.1086/187731](https://doi.org/10.1086/187731)
- . 1996, ApJL, 467, L93, doi: [10.1086/310201](https://doi.org/10.1086/310201)

- Kramer, M., Stairs, I. H., Manchester, R. N., et al. 2006, *Science*, 314, 97, doi: [10.1126/science.1132305](https://doi.org/10.1126/science.1132305)
- Lam, M. T., Cordes, J. M., Chatterjee, S., et al. 2016, *ApJ*, 821, 66, doi: [10.3847/0004-637X/821/1/66](https://doi.org/10.3847/0004-637X/821/1/66)
- Lam, M. T., Ellis, J. A., Grillo, G., et al. 2018, *ApJ*, 861, 132, doi: [10.3847/1538-4357/aac770](https://doi.org/10.3847/1538-4357/aac770)
- Lazarus, P., Karuppusamy, R., Graikou, E., et al. 2016, *MNRAS*, 458, 868, doi: [10.1093/mnras/stw189](https://doi.org/10.1093/mnras/stw189)
- Lenc, E., Murphy, T., Lynch, C. R., Kaplan, D. L., & Zhang, S. N. 2018, *MNRAS*, 478, 2835, doi: [10.1093/mnras/sty1304](https://doi.org/10.1093/mnras/sty1304)
- Lentati, L., Kerr, M., Dai, S., et al. 2017, *MNRAS*, 466, 3706, doi: [10.1093/mnras/stw3359](https://doi.org/10.1093/mnras/stw3359)
- Levin, L., McLaughlin, M. A., Jones, G., et al. 2016, *ApJ*, 818, 166, doi: [10.3847/0004-637X/818/2/166](https://doi.org/10.3847/0004-637X/818/2/166)
- Lorimer, D. R., Bailes, M., McLaughlin, M. A., Narkevic, D. J., & Crawford, F. 2007, *Science*, 318, 777, doi: [10.1126/science.1147532](https://doi.org/10.1126/science.1147532)
- Lorimer, D. R., & Kramer, M. 2004, *Handbook of Pulsar Astronomy*, Vol. 4 (Cambridge university press), 54–84
- Lower, M. E., Bailes, M., Shannon, R. M., et al. 2020, *MNRAS*, doi: [10.1093/mnras/staa615](https://doi.org/10.1093/mnras/staa615)
- Lynch, R. S., Swiggum, J. K., Kondratiev, V. I., et al. 2018, *ApJ*, 859, 93, doi: [10.3847/1538-4357/aabf8a](https://doi.org/10.3847/1538-4357/aabf8a)
- Lyne, A., Hobbs, G., Kramer, M., Stairs, I., & Stappers, B. 2010, *Science*, 329, 408, doi: [10.1126/science.1186683](https://doi.org/10.1126/science.1186683)
- Lyne, A. G. 1971, *MNRAS*, 153, 27P, doi: [10.1093/mnras/153.1.27P](https://doi.org/10.1093/mnras/153.1.27P)
- . 1984, *Nature*, 310, 300, doi: [10.1038/310300a0](https://doi.org/10.1038/310300a0)
- Madison, D. R., Cordes, J. M., Arzoumanian, Z., et al. 2019, *ApJ*, 872, 150, doi: [10.3847/1538-4357/ab01fd](https://doi.org/10.3847/1538-4357/ab01fd)
- Manchester, R. N., Hobbs, G. B., Teoh, A., & Hobbs, M. 2005, *AJ*, 129, 1993, doi: [10.1086/428488](https://doi.org/10.1086/428488)
- Martinez, J. G., Stovall, K., Freire, P. C. C., et al. 2015, *ApJ*, 812, 143, doi: [10.1088/0004-637X/812/2/143](https://doi.org/10.1088/0004-637X/812/2/143)
- McKee, J. W., Lyne, A. G., Stappers, B. W., Bassa, C. G., & Jordan, C. A. 2018, *MNRAS*, 479, 4216, doi: [10.1093/mnras/sty1727](https://doi.org/10.1093/mnras/sty1727)
- McKee, J. W., Janssen, G. H., Stappers, B. W., et al. 2016, *MNRAS*, 461, 2809, doi: [10.1093/mnras/stw1442](https://doi.org/10.1093/mnras/stw1442)
- McLaughlin, M. A., Lyne, A. G., Lorimer, D. R., et al. 2006, *Nature*, 439, 817, doi: [10.1038/nature04440](https://doi.org/10.1038/nature04440)
- Michilli, D., Hessels, J. W. T., Donner, J. Y., et al. 2018, *MNRAS*, 476, 2704, doi: [10.1093/mnras/sty368](https://doi.org/10.1093/mnras/sty368)
- Naidu, A., Joshi, B. C., Manoharan, P. K., & Krishnakumar, M. A. 2015, *ExA*, 39, 319, doi: [10.1007/s10686-015-9450-5](https://doi.org/10.1007/s10686-015-9450-5)
- Naidu, A., Joshi, B. C., Manoharan, P. K., & KrishnaKumar, M. A. 2017, *A&A*, 604, A45, doi: [10.1051/0004-6361/201629937](https://doi.org/10.1051/0004-6361/201629937)
- Naidu, A., Joshi, B. C., Manoharan, P. K., & Krishnakumar, M. A. 2018, *MNRAS*, 475, 2375, doi: [10.1093/mnras/stx3284](https://doi.org/10.1093/mnras/stx3284)
- Ng, C., & CHIME/Pulsar Collaboration. 2017, in IAUS, 2018IAUS 337, 179–182. <https://arxiv.org/abs/1711.02104>
- Ng, C., Pandhi, A., Naidu, A., et al. 2020a, *MNRAS*, 496, 2836, doi: [10.1093/mnras/staa1658](https://doi.org/10.1093/mnras/staa1658)
- Ng, C., Wu, B., Ma, M., et al. 2020b, *ApJ*, 903, 81, doi: [10.3847/1538-4357/abb94f](https://doi.org/10.3847/1538-4357/abb94f)
- Nice, D., Demorest, P., Stairs, I., et al. 2015, *Tempo: Pulsar timing data analysis*. <http://ascl.net/1509.002>
- Parent, E., Kaspi, V. M., Ransom, S. M., et al. 2018, *ApJ*, 861, 44, doi: [10.3847/1538-4357/aac5f0](https://doi.org/10.3847/1538-4357/aac5f0)
- Pen, U. L., Macquart, J. P., Deller, A. T., & Brisken, W. 2014, *MNRAS*, 440, L36, doi: [10.1093/mnrasl/slu010](https://doi.org/10.1093/mnrasl/slu010)
- Perera, B. B. P., Stappers, B. W., Weltevrede, P., Lyne, A. G., & Rankin, J. M. 2016, *MNRAS*, 455, 1071, doi: [10.1093/mnras/stv2403](https://doi.org/10.1093/mnras/stv2403)
- Perera, B. B. P., DeCesar, M. E., Demorest, P. B., et al. 2019, *MNRAS*, 490, 4666, doi: [10.1093/mnras/stz2857](https://doi.org/10.1093/mnras/stz2857)
- Petroff, E., Hessels, J. W. T., & Lorimer, D. R. 2019, *A&A Rv*, 27, 4, doi: [10.1007/s00159-019-0116-6](https://doi.org/10.1007/s00159-019-0116-6)
- Price, D. C., Staveley-Smith, L., Bailes, M., et al. 2016, *JAI*, 5, 1641007, doi: [10.1142/S2251171716410075](https://doi.org/10.1142/S2251171716410075)
- Radhakrishnan, V., & Manchester, R. N. 1969, *Nature*, 222, 228, doi: [10.1038/222228a0](https://doi.org/10.1038/222228a0)
- Ransom, S. 2011, PRESTO: Pulsar Exploration and Search TOOlkit. <http://ascl.net/1107.017>
- Rea, N., Esposito, P., Pons, J. A., et al. 2013, *ApJL*, 775, L34, doi: [10.1088/2041-8205/775/2/L34](https://doi.org/10.1088/2041-8205/775/2/L34)
- Reardon, D. J., Coles, W. A., Hobbs, G., et al. 2019, *MNRAS*, 485, 4389, doi: [10.1093/mnras/stz643](https://doi.org/10.1093/mnras/stz643)
- Shapiro, I. I. 1964, *PhRvL*, 13, 789, doi: [10.1103/PhysRevLett.13.789](https://doi.org/10.1103/PhysRevLett.13.789)
- Sobey, C., Bilous, A. V., Grießmeier, J. M., et al. 2019, *MNRAS*, 484, 3646, doi: [10.1093/mnras/stz214](https://doi.org/10.1093/mnras/stz214)
- Spitler, L. G., Scholz, P., Hessels, J. W. T., et al. 2016, *Nature*, 531, 202, doi: [10.1038/nature17168](https://doi.org/10.1038/nature17168)
- Stairs, I. H. 2003, *LRR*, 6, 5, doi: [10.12942/lrr-2003-5](https://doi.org/10.12942/lrr-2003-5)
- Stairs, I. H., Lyne, A. G., Kramer, M., et al. 2019, *MNRAS*, 485, 3230, doi: [10.1093/mnras/stz647](https://doi.org/10.1093/mnras/stz647)
- Stovall, K., Lynch, R. S., Ransom, S. M., et al. 2014, *ApJ*, 791, 67, doi: [10.1088/0004-637X/791/1/67](https://doi.org/10.1088/0004-637X/791/1/67)
- Thompson, A. R., Moran, J. M., & Swenson, George W., J. 2001, *Interferometry and Synthesis in Radio Astronomy*, 2nd Edition (Springer, Cham), 59–88
- Thornton, D., Stappers, B., Bailes, M., et al. 2013, *Science*, 341, 53, doi: [10.1126/science.1236789](https://doi.org/10.1126/science.1236789)

- Tiburzi, C., Verbiest, J. P. W., Shaifullah, G. M., et al. 2019, MNRAS, 487, 394, doi: [10.1093/mnras/stz1278](https://doi.org/10.1093/mnras/stz1278)
- van Straten, W. 2006, ApJ, 642, 1004, doi: [10.1086/501001](https://doi.org/10.1086/501001)
- van Straten, W., & Bailes, M. 2011, PASA, 28, 1, doi: [10.1071/AS10021](https://doi.org/10.1071/AS10021)
- van Straten, W., Bailes, M., Britton, M., et al. 2001, Nature, 412, 158, doi: [10.1038/35084015](https://doi.org/10.1038/35084015)
- van Straten, W., Demorest, P., & Oslowski, S. 2012, AR&T, 9, 237. <https://arxiv.org/abs/1205.6276>
- Verbiest, J. P. W., Lentati, L., Hobbs, G., et al. 2016, MNRAS, 458, 1267, doi: [10.1093/mnras/stw347](https://doi.org/10.1093/mnras/stw347)
- Wang, N., Manchester, R. N., Johnston, S., et al. 2005, MNRAS, 358, 270, doi: [10.1111/j.1365-2966.2005.08798.x](https://doi.org/10.1111/j.1365-2966.2005.08798.x)
- Wang, N., Yan, Z., Manchester, R. N., & Wang, H. X. 2008, MNRAS, 385, 1393, doi: [10.1111/j.1365-2966.2008.12864.x](https://doi.org/10.1111/j.1365-2966.2008.12864.x)
- Weltevrede, P., Johnston, S., & Espinoza, C. M. 2011, in AIPC, Vol. 1357, 109–112, doi: [10.1063/1.3615091](https://doi.org/10.1063/1.3615091)
- Yu, H.-R., Zhang, T.-J., & Pen, U.-L. 2014, PhRvL, 113, 041303, doi: [10.1103/PhysRevLett.113.041303](https://doi.org/10.1103/PhysRevLett.113.041303)